M. Bechini, M.B. Quadrelli, M. Lavagna, J.J. Wang
Hovering of an Electrically Actuated Spacecraft in a Small-Body Plasma Field
Journal of Spacecraft and Rockets, In press - Published online 03/06/2021
doi:10.2514/1.A34954

Hovering of an Electrically Actuated Spacecraft in a Small Body Plasma Field

Michele Bechini *
Politecnico di Milano, Milano, Italy, 20156

Marco B. Quadrelli †
Jet Propulsion Laboratory, California Institute Technology, Pasadena, CA 91109

Michèle Lavagna ‡
Politecnico di Milano, Milano, Italy, 20156

Joseph J. Wang §
University of Southern California, Los Angeles, CA 90089

The paper presents simulation models and an analysis of the hovering capability of an electrostatic spacecraft around a small celestial body. The hovering capabilities of an electrically actuated spacecraft are evaluated by combining orbital dynamics analysis with three-dimensional fully kinetic particle-in-cell simulations of asteroid/spacecraft interactions with the solar wind plasma. The zero velocity curves obtained from the analysis allow the identification of the equilibrium points for different levels of charge. The analysis of the system equilibria indicates the presence of equilibrium points in the combined gravitational, electrostatic, and solar illumination field, most of which can be obtained by charging the spacecraft negatively. The charge-to-mass ratio needed to hover is obtained for different orbital positions, and an analysis of the sensitivity of the equilibria with respect to the spacecraft equivalent radius and with respect to the Sun-to-Main Body distance provides additional insight into the system dynamics.

Nomenclature

d Main-Body-to-Sun distance, m

h Angular Momentum, m^2/s

a Semi-Major Axis, m

e Eccentricity, -

*PhD Candidate, Politecnico di Milano Department of Aerospace Science and Technology, Via La Masa, 34, 20156, Milano, Italy. Email: michele.bechini@polimi.it

†Principal and Group Supervisor, Robotics Modeling and Simulation Group, Jet Propulsion Laboratory, California Institute Technology, M/S 198-219, 4800 Oak Grove Drive, Pasadena, CA 91109. Email: marco.b.quadrelli@jpl.nasa.gov

‡Professor, Politecnico di Milano Department of Aerospace Science and Technology, Via La Masa, 34, 20156, Milano, Italy. Email: michelle.lavagna@polimi.it

§Professor, Department of Astronautical Engineering, University of Southern California, Los Angles, CA 90089. Email: josephjw@usc.edu

P Semilatus Rectum, m

θ True Anomaly, deg

μ Gravitational Parameter, m^3/s^2

M Mass, Kg

f Force, N

N Orbital Angular Velocity, rad/s

ω Angular Velocity, rad/s

$\mathbf{J}$ Mass Moment of Inertia Matrix

$\mathbf{T}$ Torque Vector

$\mathbf{a}$ Acceleration Vector

$\mathbf{v}$ Velocity Vector

$\mathbf{r}$ Position Vector

$\mathbf{G}$ Gradient Tensor of a Vector Field

C Solar Radiation Pressure Coefficient

$\mathbf{E}$ Electric Field Vector, V

q Single Charge, C

Q Total Net Charge, C

$\boldsymbol{S}_q$ First Moment of Charge Vector

$\boldsymbol{I}_q$ Second Moment of Charge Tensor

Subscript

a Asteroid

s Sun

SC Spacecraft

g Gravitational

p Solar Radiation Pressure

pa Absorption

ps Specular Reflection

pd Diffuse Reflection

e Electrostatic

x, y, z General components of vector/tensor

Superscript (for Rotation Matrices the Super- and Sub-Scripts refer to this list)

r Radial/In-Track/Cross-Track (RIC) Frame

a Asteroid-Centered Inertial (ACI) Frame

b Body Fixed (BF) Frame

I. Introduction

The Electrostatic Glider (or E-Glider), developed at NASA Jet Propulsion Laboratory [1], is a novel spacecraft concept. It was inspired by the observed behavior of small spiders (named *Gossamer Spiders*). A gossamer spider produces charged threads that are mutually repelled (creating a sort of "hot-air balloon" made by thin threads) due to the presence of the electric charge which interacts with the Earth's static atmospheric electric field, generating a lift component on the spider itself [2]. This *ballooning effect* is effective also in the absence of convection or aerodynamics effects. Similar to a gossamer spider, an E-Glider utilizes the spacecraft charging level and the resulting electrostatic interactions with the charged plasma in the vicinity of a charged planetary body for orbiting and maneuvering. In particular, the E-Glider can lead to advantageous propulsion and navigation capabilities for exploring small airless bodies in the solar system (asteroids and comets, called Small Bodies in this paper) over existing technologies.

Small airless bodies represent the next frontier in solar system explorations. Recent observations have demonstrated the important role of Small Bodies in the origin of the solar system and in astrobiology [1]. Moreover, the National Research Council (US) stated that the development of new technologies for Small Bodies mobility should be of high priority for NASA [3]. In-situ analyses of Small Bodies are limited by the knowledge of the surface terrain and vehicle mobility. The mobility of all current robotics and human exploration systems relies on the interaction between the system and the target body surface. Several studies revealed that the surface of Small Bodies can have extremely complex landscapes covered by a regolith layer and/or big boulders [4, 5]. Several advanced vehicle concepts have been proposed recently for bodies with significant gravity levels, such as the DuAxel vehicle [6] capable of moving on extremely challenging surfaces and the recently assembled small helicopter, the *Mars Ingenuity Helicopter*, capable of flying in the Mars' atmosphere [7]. However, despite their unique capabilities, these vehicle concepts are still not ideal for applications on a small airless body due to the extreme conditions for mobility, as described next.

The environment presented by Small Bodies is highly challenging [1]. Due to the small size and extremely irregular shape presented by some asteroids, the gravity field can be highly irregular, and of very small intensity, especially on the surface [5, 8]. The combined effects of the irregularity of the gravity field and the low intensity of the gravitational acceleration produced by these bodies (milli-G order of magnitude [1]) make the orbital environment highly perturbed [9], leading to non-Keplerian orbits. The solar radiation pressure can also have a strong impact on the vehicle dynamics [8, 10]. As a result, the escape velocities from the small bodies are particularly low [11, 12]. For these reasons, the physics of vehicles that operate in the micro-gravity environment of small bodies are very different from conventional

planetary landers and orbiters in a high intensity and regular gravity field, requiring special precautions during the design phase. Currently, the only options for achieving the mobility in such environments are some forms of hoppers, grippers, and hybrid systems [13, 14].

A promising idea is to take advantage of the natural environment near the airless bodies, instead of fighting it. A vehicle like the E-Glider provides a new alternative by hovering over the surface of small bodies for proximity observations and measurements, while exploiting the naturally charged particle environment near the surface to produce lift [1]. The electrostatic interaction between charged bodies, a well-known phenomenon of classical physics, has been considered for various space applications in recent years, such as docking, formation flying, collision avoidance, and attitude control [1, 15–17]. These applications, however, differ from the E-Glider concept because all of them rely on the realization of artificially generated Coulomb forces between two (or more) spacecraft. Conversely, the E-Glider interacts directly with the electrostatic field of the target body. Without a global magnetic field and an atmosphere, airless bodies are directly exposed to the solar wind plasma and to the sunlight and are thus electrically charged by the solar wind plasma impingement and by the emission of photoelectrons and secondary electrons [18, 19]. A spacecraft around a small airless body is also electrically charged by the same process. By manipulating the charging state of an E-Glider and thus the net electrostatic force with respect to the charged ambient medium, an E-Glider may achieve complex orbital maneuvers.

Many studies have been carried out to investigate the interactions between asteroids and the solar wind plasma, and asteroid charging [18, 20–22]. The solar wind plasma is in a state of mesothermal flow (i.e. the directed plasma flow speed is larger than ion thermal speed but less than electron thermal speed). An asteroid in the solar wind creates a plasma wake behind it, within which the ion current is reduced to a fraction of its ambient level [23, 24]. Both solar illumination and the solar wind plasma flow will have a substantial influence on the potential of the asteroid surface, which is determined by the local current balance condition. The potential of the illuminated surface is expected to be slightly positive with respect to the ambient solar wind due to the emission of the photoelectrons, while that of the shadowed surface can be easily charged to a very negative potential due to a lack of ion current collection [22]. Previously, Nitter et al. derived in [20] an analytical solution for one-dimensional (1D) plasma sheath around an asteroid. Based on [20], a multi-sheath analytical asteroid charging model was obtained by relaxing some hypotheses [25] and by including the effects of drifting electrons [26]. This simplified model was used in early E-Glider analyses [1, 27, 28]. Recently, Wang et al. developed in [4, 22, 29] a three-dimensional (3D) fully kinetic immersed-finite-element particle-in-cell (USC-IFEPIC) simulation model to simulate plasma interactions and charging of irregularly shaped, composite asteroids. In this paper, the USC-IFEPIC model is applied to obtain the electric field around a small asteroid, leading to a much more accurate analysis of the hovering capabilities of the E-Glider compared to the earlier results obtained with the much simplified 1D model.

In [1], a preliminary study of the levitation capabilities was carried out under the strongly restrictive assumptions of

the analytical asteroid electric field model derived from [20]. 3D Computer Aided Design models were developed and used in the simulations implemented at JPL to evaluate the orbital dynamics in a non-spherical highly irregular micro-gravity environment (similar to 25143 Itokawa). Most importantly, a navigation system based on a "minimum-potential" approach was proposed, involving autonomous path planning. In this initial work, two different day-side fuel-free operations were developed [28]: the electrostatic hovering and the electrostatic orbiting. Since the E-Glider leverages the natural charging for propulsion, fuel cost is minimal, and the concept offers strong advantages from the mass budget viewpoint. Moreover, the operations on the day-side provide improvements with respect to the natural orbiting from the optical observation and the power generation point of view. By including also the contribution of the electrostatic force beyond the solar and gravitational forces, the presence of new equilibrium points was determined, in particular on the sunlit side (not present in the natural dynamics). The initial spacecraft model used for the analysis was composed of four big spherical electrodes. For this configuration, the computation showed that the E-Glider potential needed for hovering is of the order of tens of kV, a value prohibitive for a real mission. In order to solve this problem, a new class of orbits, named *electrostatic periodic orbits*, was proposed in [28]. The effects of the irregularity from an ellipsoidal body on the gravitational and electrostatic field were also evaluated. The analysis of the attitude dynamics of a rigid body was also carried out by deriving an analytical formulation obtained by including the electrostatic torque in addition to the gravity gradient torque. The attitude stability conditions obtained analytically were confirmed by numerical simulations, and stable attitude motion was proven to be achievable in electrostatic orbits under the effects of the electrostatic torque.

To achieve the desired mobility through the electrostatic interaction, an E-Glider must provide a certain amount of net charge to its electrodes. Various options to generate and control the charge were considered in [27]. Electron or ion beam emissions [30–33] are the most common methods to generate charge on-board. However, the net charge that can be generated is controlled by spacecraft charging, which can attract some of the emitted charged particles back, as well as the space charge limit of the beam, which will form a virtual electrode at the beam exit to cap the transmission of an un-neutralized beam at the space charge limit [32–34]. Other methods include the selection of materials with the desired conductivity or photoelectron emission properties [35–37] or inducing differential surface charging using biasing devices such as batteries or small Van De Graaff generators [38]. To determine the charge carried by an E-Glider, a detailed analysis of the capacitance and charging mechanism is needed. This is beyond the scope of this paper. The objective of this study is to carry out a baseline analysis of the hovering capability. Hence, in this paper, the charge carried by an E-Glider is treated as an input parameter, and the hovering capability is analyzed as a function of the E-Glider charge to mass ratio.

The electric field obtained from the PIC simulations described in [4, 22, 39] was included for the first time in the analyses presented in [40], where an electrostatic feedback control of a spacecraft was also developed under highly restrictive assumptions. The most interesting analysis presented in [40] is an evaluation of the power required and the potential reached by several electrode geometries in a static plasma. The sensitivity analysis developed and the results

obtained relate the power consumption with the mass of the spacecraft and with the charge over mass ratio. A significant power reduction is obtained for wire electrodes with respect to the spherical electrodes [28].

A preliminary sizing for an E-Glider immersed in the Martian atmosphere highlighted that the high level of potential reached by the electrodes can overcome the limits imposed by the atmospheric breakdown voltage, which is the most limiting factor to enable planetary applications. Hence, in principle, the E-Glider can also operate in a much denser plasma at ionospheric conditions.

The theory of the E-Glider based on the Nitter model, as outlined in [1] and [28], suggested several new mission concepts based on the electrostatic interaction of the spacecraft with the environment surrounding a small airless body. The novelties represented by first-principle based IFEPIC simulations of solar wind plasma interaction with asteroid surface suggest that a re-evaluation of the results in [1, 28] would be necessary in order to obtain a more accurate assessment of the E-Glider's capabilities for real missions. This paper presents a more detailed investigation of the hovering capabilities of E-Glider near a small airless body which utilizes the results of the electrostatic interactions obtained from fully kinetic IFEPIC simulations, thus leading to a generalization of the previously obtained results.

II. E-Glider Dynamics

A. Reference Frames

The definition of the notation and the reference frames used is necessary to correctly understand the dynamic models and the equations of motion explained in the following paragraphs. The notation used to express the vectors and the matrices in the different reference frames is the following:

- ${}^{a}\mathbf{x}$ stands for a vector or a tensor $\mathbf{x}$ expressed in the a-frame
- ${}^{a}\omega_{bc}$ stands for the angular velocity of c-frame with respect to b-frame expressed in the a-frame
- ${}^{a}\mathbf{R}_{b}$ stands for the rotation matrix (or tensor) $\mathbf{R}$ which converts ${}^{b}\mathbf{x}$ into ${}^{a}\mathbf{x}$, thus ${}^{a}\mathbf{x} = {}^{a}\mathbf{R}_{b}{}^{b}\mathbf{x}$

1. Main Body Centered Reference Frames

Radial/In-Track/Cross-Track (RIC) Frame - r

The Radial/In-Track/Cross-Track (RIC) reference frame is the reference frame used to write the translation equations of motion. This is a non-inertial reference frame.

The RIC frame is defined as (see Fig. 1):

- O = origin at the Main Body center of mass
- X = axis directed away from the Solar System Barycenter (e.g. along the radial direction)
- Y = axis lying on the orbital plane and completing the right-handed orthogonal frame (e.g. along the in-track direction)

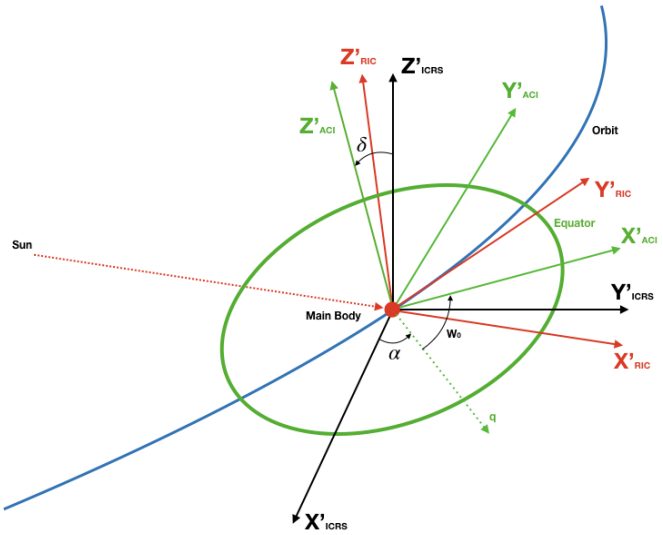

Fig. 1 Main Body Centered Reference Frames - ACI and RIC

- Z = axis parallel to the orbital angular momentum vector (e.g. along the cross-track direction)

The RIC can be derived from the perifocal reference frame by translating it from the barycenter of the Solar System to the Main Body center of mass and then by applying a rotation equal to the true anomaly of the Main Body as ${}^{r}\mathbf{R}_{p} = [\Theta(t)]_3$.

Asteroid-Centered Inertial (ACI) Frame - a

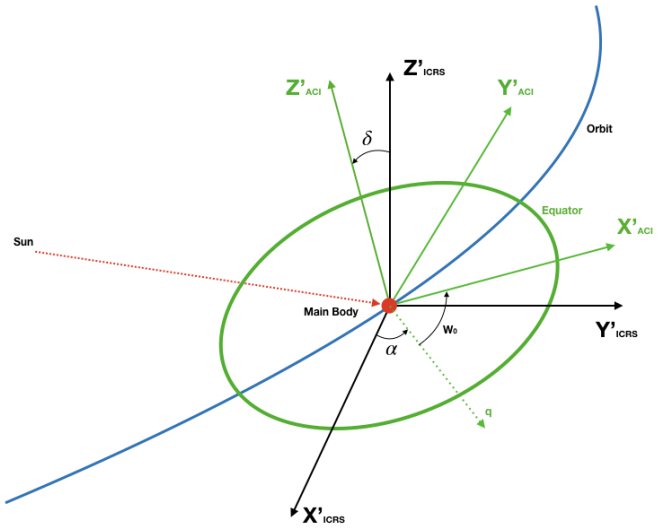

Fig. 2 ACI Reference Frame

The Asteroid-Centered Inertial (ACI) reference frame helps to define the attitude and the rotations of both the

spacecraft and the Main Body. This reference frame can be assumed to be inertial when the attitude refers to it (the non-inertial components are due to the translational motion).

This reference frame can be defined as (see Fig. 2):

- O = origin at the Main Body center of mass
- X = axis lying on the equator and pointing towards the prime meridian at the reference epoch
- Y = axis lying on the equator and completing the right-handed orthogonal frame
- Z = axis directed as the Main Body rotation angular momentum vector

The ACI reference frame can be derived by translating the International Celestial Reference Frame on the Main Body and then rotating it as ${}^{a}\mathbf{R}_i = [W_0]_3[\delta]_1[\alpha]_3$, where W_0 is the position of the prime meridian at a given epoch, δ is the declination of the positive pole and α is the right ascension of the positive pole (see Fig. 2).

2. Spacecraft Centered Reference Frames

Body Fixed (BF) Frame - b

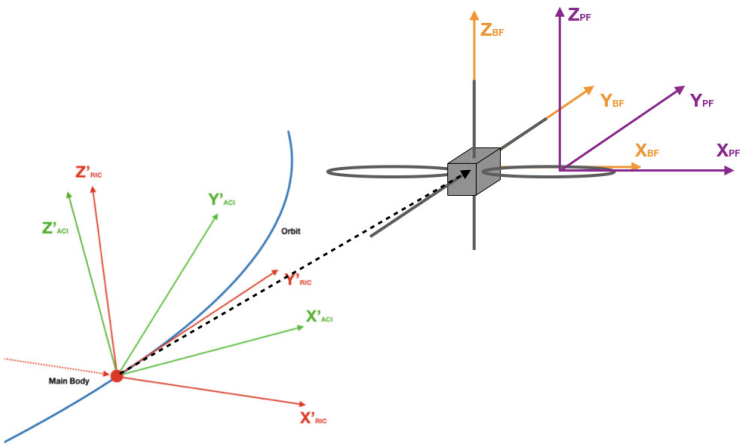

Fig. 3 Spacecraft Centered Reference Frames - BF and PF

The Body Fixed (BF) reference frame is rigidly "attached" to the spacecraft. The propagation of the attitude equations of motion is carried out in this reference frame. We assumed the attitude and the rotation rates considered as expressed in the BF frame and related to the ACI frame.

The definition of the BF reference frame is (see Fig. 3):

- O = origin at the Spacecraft center of mass
- Axes = defined by the geometry of the spacecraft (usually oriented towards the principal axes of inertia)

The spacecraft attitude quaternion ${}^{b}\mathbf{q}_a$ defines its orientation with respect to the ACI frame.

B. Equations of Motion

In the ensuing paragraph, we derive the equations of motion both for the case of Clohessy-Wiltshire formulation, suitable for a main body with almost circular orbits, and for the case of the more accurate "full dynamic" formulation, which can be applied also to small bodies that are on orbits with high eccentricity.

1. Translation Dynamics

Full Model Three-Body Probelm

The linearized equations of motion are obtained by considering the Main Body as a target and the E-Glider as the chaser, while the Sun is the third body in the full model case. The derivation of the equations of motion is carried out in the RIC reference frame, thus the distance of the target from the Sun and both the angular velocity and the angular acceleration with respect to the Sun are needed to derive the correct formulation. We assume the case of "proximity flight" [11] in the derivation of the equations of motion, thus the distance of the spacecraft from the Sun and the distance of the Main Body from the Sun are comparable and the distance of the spacecraft from the Main Body is much less than the previous two distances. By knowing the Keplerian parameters of the Main Body orbit around the Sun and $\theta = \theta(t)$, the equations applied in the computation of the distance d of the Main Body from the Sun, and the instantaneous asteroid orbital angular velocity and angular acceleration $\dot{\theta}$ and $\ddot{\theta}$ are:

$$d = \frac{h_a^2}{\mu_s} \cdot \frac{1}{1 + e_a cos\theta} = \frac{P_a}{1 + e_a cos\theta} \tag{1}$$

$$\dot{\theta} = \frac{h_a^2}{d^2} = \frac{\sqrt{P_a \mu_s}}{d^2} \tag{2}$$

$$\ddot{\theta} = -2\sqrt{\frac{\mu_s}{P_a}} \cdot \frac{e_a sin\theta\dot{\theta}}{d} = -2\frac{e_a \dot{\theta}^2 sin\theta}{1 + e_a cos\theta} \tag{3}$$

For the sake of clarity, please notice that Eq. (3) can be obtained by differentiating Eq. (2) with respect to time and then by substituting in it the formulation used to compute the distance given in Eq. (1).

The angular velocity vector of the Main Body about the Sun is $\mathbf{\Omega}$ and it has a constant direction taken to be in the Z-direction in perifocal (PQW) frame, thus $\mathbf{\Omega}$ is also the angular velocity of the RIC frame with respect to the PQW frame. The magnitude of $\mathbf{\Omega}$ follows Eq. (2). Moreover ${}^r\mathbf{\Omega} = (0, 0, \dot{\theta})$ and ${}^r\dot{\mathbf{\Omega}} = (0, 0, \ddot{\theta})$ can be easily verified. We need the spacecraft acceleration in RIC frame to write the translation dynamical equation of motion in this reference frame. Let $\mathbf{r}$ be the position vector of the spacecraft with respect to the Main Body, while $\mathbf{D}_s$ and $\mathbf{D}_a$ are the position vectors of the spacecraft with respect to the Sun and of the Main Body with respect to the Sun respectively, as shown in Fig. 4. By knowing that $\mathbf{D}_s = \mathbf{D}_a + \mathbf{r}$, the absolute acceleration can be obtained after some mathematical steps as [41]:

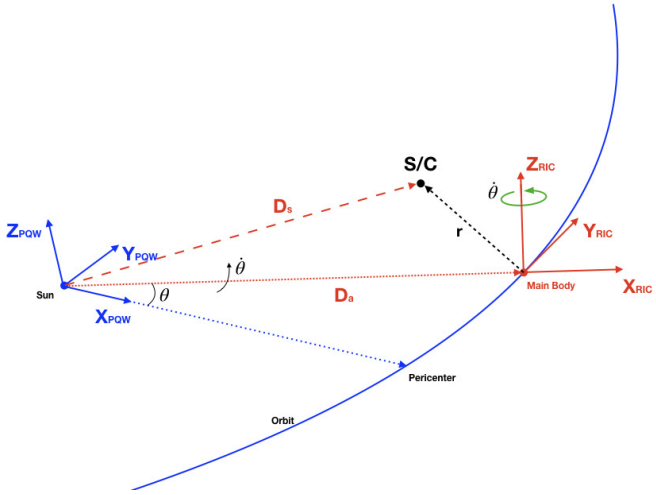

Fig. 4 Full Model reference frames and vectors

$$\ddot{\mathbf{D}}_s = \ddot{\mathbf{D}}_a + \mathbf{a} + \dot{\boldsymbol{\Omega}} \times \mathbf{r} + \boldsymbol{\Omega} \times \boldsymbol{\Omega} \times \mathbf{r} + 2\boldsymbol{\Omega} \times \mathbf{v} \tag{4}$$

where $\mathbf{r}$, $\mathbf{v}$ and $\mathbf{a}$ are in RIC frame. $\dot{\boldsymbol{\Omega}} \times \mathbf{r}$ is the term related to the angular acceleration of the frame, while $\boldsymbol{\Omega} \times \boldsymbol{\Omega} \times \boldsymbol{r}$ and $2\boldsymbol{\Omega} \times \mathbf{v}$ are the centrifugal term and the Coriolis acceleration respectively. By solving Eq. (4) for the relative acceleration $\mathbf{a}$ in RIC and by knowing that $\ddot{\mathbf{r}} = \ddot{\mathbf{D}}_s - \ddot{\mathbf{D}}_a$, we obtain:

$$\mathbf{a} = {}^{p}\ddot{\mathbf{r}} - \dot{\boldsymbol{\Omega}} \times \mathbf{r} - \boldsymbol{\Omega} \times \boldsymbol{\Omega} \times \mathbf{r} - 2\boldsymbol{\Omega} \times \mathbf{v} \tag{5}$$

The vector ${}^{p}\ddot{\mathbf{r}}$ measured in the inertial frame must be computed to define the relative acceleration in the RIC frame (the co-moving one). To do that, a linearized model can be used. The linearized model is valid since $r \ll D_s, D_a$. Recalling that $\ddot{\mathbf{D}}_a = -\frac{\mu_s}{D_a^3}\mathbf{D}_a$, the equations of motion of the chaser relative to the target measured in the PQW inertial frame can be derived after some mathematical steps, neglecting the higher order terms, as:

$$\ddot{\mathbf{r}} = -\frac{\mu_s}{D_a^3}\left[\mathbf{r} - \frac{3}{D_a^2}\left(\mathbf{D}_a \cdot \mathbf{r}\right)\mathbf{D}_a\right] \tag{6}$$

By expressing $\mathbf{r}$ and $\mathbf{D}_a$ in the co-moving RIC frame and by substituting the result into Eq. (5), the equation of motion for translation for the full model in RIC frame can be obtained by introducing the term $\frac{{}^{r}\mathbf{f}}{M}$, which gives the effects of the active forces acting on the spacecraft. Hence, in the RIC frame, we obtain:

$$ {}^{r}\mathbf{a} = \frac{{}^{r}\mathbf{f}}{M} - \frac{\mu_s}{d^3}\begin{bmatrix} -2r_x \\ +r_y \\ +r_z \end{bmatrix} + \ddot{\theta}\begin{bmatrix} r_y \\ -r_x \\ 0 \end{bmatrix} + \dot{\theta}^2\begin{bmatrix} +r_x \\ +r_y \\ 0 \end{bmatrix} + 2\dot{\theta}\begin{bmatrix} +v_y \\ -v_x \\ 0 \end{bmatrix} \tag{7} $$

$$ {}^{r}\dot{\mathbf{r}} = {}^{r}\mathbf{v} \tag{8} $$

For the purposes of this work the Main Body gravitational perturbation effects, the Solar Radiation Pressure Force, and the Spacecraft Electrostatic interactions with the plasma field are considered. The active forces components derivations are available in dedicated sections (Sec. II.C, II.D, II.E).

Clohessy-Wiltshire Three-Body Probelm

The Clohessy Wiltshire formulation can be derived by assuming the target (the Main Body) to be on a circular unperturbed orbit around the third body (the Sun). This strong assumption allows us to consider the mean motion of the Main Body as constant, hence $\dot{\theta} = N = \text{const}$. Moreover, $e = 0$ for a circular orbit, thus the angular momentum can be written as $h_a = \sqrt{\mu_s D_a}$. By using these relations and by knowing that, since $N = \text{const}$, the term related to $\dot{\Omega}$ is null, the translation dynamical equation in the RIC frame (Eq. (7)) can be rewritten by using the Clohessy-Wiltshire approximation as:

$$ {}^{r}\mathbf{a} = \frac{{}^{r}\mathbf{f}}{M} + 2N\begin{bmatrix} +v_y \\ -v_x \\ 0 \end{bmatrix} + N^2\begin{bmatrix} +3r_x \\ 0 \\ -r_z \end{bmatrix} \tag{9} $$

$$ {}^{r}\dot{\mathbf{r}} = {}^{r}\mathbf{v} \tag{10} $$

The external terms considered are the Main Body gravitational perturbation effects, the Solar Radiation Pressure Force, and the Spacecraft Electrostatic interactions with the plasma field. The active forces components derivations are described later (Sec. II.C, II.D, II.E).

2. Attitude Dynamics

The attitude dynamics equation of motion is the classical Euler's equation used for attitude propagation. This equation can be derived from the angular momentum equation written in an inertial reference frame. The Euler's equation in BF frame is:

$$ {}^{b}\boldsymbol{J}^{b}\dot{\boldsymbol{\omega}}_{ab} = {}^{b}\boldsymbol{J}^{b}\boldsymbol{\omega}_{ab} \times {}^{b}\boldsymbol{\omega}_{ab} + {}^{b}\mathbf{T} \tag{11} $$

${}^b\boldsymbol{\omega}_{ab}$ is the angular rate of the BF frame (thus the spacecraft angular rate) with respect to the inertial reference frame (ACI) expressed in BF reference frame. The term ${}^b\mathbf{T}$ collects all the active torques applied to the spacecraft expressed in BF reference frame. In this work, the torques given by the gravity field of the Main Body, the solar radiation pressure torque and the electrostatic torque have been considered. The derivations of these components are shown later in Sec. II.C, II.D, II.E. The attitude dynamics equation must be completed by also adding the attitude kinematics. We used the quaternion parameters to represent the attitude, thus the quaternion kinematics equation can be written as:

$$ {}^b\dot{\boldsymbol{q}}_a = \frac{1}{2}\begin{bmatrix} {}^b\boldsymbol{\omega}_{ab} \\ 0 \end{bmatrix} \otimes {}^b\mathbf{q}_a \tag{12} $$

in which ${}^b\mathbf{q}_a$ is the attitude quaternion from ACI to BF reference frame and the symbol $\otimes$ stands for the quaternion product. In the simulations, the quaternion must be normalized after each integration step in order to avoid divergences.

C. Modeling of Gravitational Forces

Two different gravity field models have been considered, the classical and simple Point Mass Gravity Model and a more complex and accurate model based on the Spherical Harmonics Expansion.

Point Mass Gravity Model

The Point Mass Gravity Model is suitable for bodies with a spherical-symmetric mass distribution. If we can assume the mass of the Main Body concentrated in the center of gravity of the body itself, then the point mass gravity model is valid. This model is singularity-free and its computational cost is extremely low, thus the Point Mass Gravity Model can be used for feasibility studies and first approximation analysis. $\mathbf{f}_g$, the gravitational force acting on the spacecraft, can be simply derived by knowing that the gravitational force is conservative, thus the gravitational acceleration is $\mathbf{a}_g = \nabla U$, where U is the gravitational potential, i.e.:

$$ \mathbf{a}_g = -\frac{\mu}{r^3}\mathbf{r} \tag{13} $$

The formulation for the gravity gradient tensor $\mathbf{G}_g$ is the following [42]:

$$ \mathbf{G}_g = \nabla\mathbf{a}_g = -\frac{\mu}{r^3}\left(\mathbf{I} - \frac{3}{r^2}\mathbf{r}\otimes\mathbf{r}\right) \tag{14} $$

Notice that the symbol $\otimes$ stands for the outer product.

1. Spherical Harmonics Model

The expansion in spherical harmonics of the gravitational field is a commonly used method to compute the gravitational potential U_g. This method offers the possibility to compute the tangential components of the gravitational acceleration and to achieve an accuracy level higher than the point-mass model without introducing an excessively high computational load (e.g. as the FE MASCON method). For the analysis of an E-Glider the terminator region is of particular interest, thus a singularity-free method is required for the computation of the gravity field also at the poles. There are several singularity-free methods, the one used here is the method developed by Pines in 1973 [43] due to its accuracy and fast computations capabilities. A modified recursion formula is needed for the computation of the Legendre Polynomials to achieve also the stability required for high order gravitational models since the one originally proposed by Pines was unstable for high n [44, 45]. Hence the gravitational potential can be rewritten as:

$$U_g = \sum_{n=0}^{\infty} \rho_n \sum_{m=0}^{n} A_{n,m}(u) D_{n,m}(s,t) \tag{15}$$

The definition of ρ_n is given in [43] (see Eq. (26)) and $D_{n,m}(s,t)$ is a mass coefficient function. Equation (15) must be differentiated in Pines' reference frame in order to compute the gravitational acceleration $\mathbf{a}_g$, thus the equations for the gravitational acceleration and for the gravity gradient tensor are:

$$\mathbf{a}_g = \nabla U_g = a_1 \hat{\mathbf{i}} + a_2 \hat{\mathbf{j}} + a_3 \hat{\mathbf{k}} + a_4 \hat{\mathbf{r}} \tag{16}$$

$$\mathbf{G}_g = \nabla \mathbf{a}_g = \frac{\partial}{\partial \mathbf{r}} \left(a_1 \hat{\mathbf{i}} + a_2 \hat{\mathbf{j}} + a_3 \hat{\mathbf{k}} + a_4 \hat{\mathbf{r}} \right) \tag{17}$$

The equations to compute both the coefficients of Eq. (16) and the derived coefficients of Eq. (17) in a simple and efficient way are available in [43] and they are not reported here for the sake of brevity.

2. External Forces and Torques

The computation of both the gravitational forces and the gravitational torques acting on the spacecraft is needed, independently from the model assumed. The local acceleration $\mathbf{a}_g(\mathbf{r})$ and the local gravity gradient $\mathbf{G}_g(\mathbf{r})$ components can be computed as explained in the previous section.

External Forces

In the analysis the spacecraft can be considered either as an extended single body (hence with a single mass and a single inertia), or as an ensemble of parts (multibody approach) with their own mass localized in the center of mass of the part itself. A linear model can be assumed in the case of a satellite modeled as an extended body. In this case the vector $\boldsymbol{\rho} = \mathbf{r} - \mathbf{r}_0$, in which $\mathbf{r}_0$ is the position of the center of mass, gives the position of a point with respect to the center of mass of the spacecraft, thus the approximated equation for the gravitational acceleration is:

$$\mathbf{a}_g(\mathbf{r}) = \mathbf{a}_g(\mathbf{r}_0) + \mathbf{G}_g(\mathbf{r}_0)\boldsymbol{\rho} \tag{18}$$

By integrating Eq. (18) and by remembering that $\int_{S/C} \boldsymbol{\rho} dM$ is the first moment of mass about the center of mass itself, hence null by definition, the gravitational force becomes:

$$\mathbf{f}_g = \mathbf{a}_g(\mathbf{r}_0)M \tag{19}$$

In the case of a spacecraft modeled as an ensemble of parts, the total gravitational force acting on the whole spacecraft can be computed as the summation of the forces acting on each part constituting the spacecraft. By referring with the index i to the i-th part, the gravitational force is:

$$\mathbf{f}_g = \sum_i \left(\int_{\text{i-th part}} \mathbf{a}_g(\mathbf{r}_i) dM_i \right) = \sum_i \left(\mathbf{a}_g(\mathbf{r}_i) M_i \right) \tag{20}$$

where $\mathbf{r}_i$ and M_i are the position of the center of mass and the mass of the i-th part respectively. This method has a stronger impact on the computational load with respect to the previous one, but it allows a higher level of precision for highly extended bodies (where the linearized model of the first case is no longer valid).

External Torques

For the case of a single extended body, by using the very same assumptions of the previous paragraph, the equation for the gravity torque is:

$$\mathbf{T}_g = \int_{S/C} \boldsymbol{\rho} \times (\mathbf{a}_g(\mathbf{r}_0) + \mathbf{G}_g(\mathbf{r}_0)\boldsymbol{\rho}) dM \tag{21}$$

By remembering that, once again, $\int_{S/C} \boldsymbol{\rho} dM$ is the first moment of mass about the center of mass itself, hence null by definition, we can obtain:

$$\mathbf{T}_g = \int_{S/C} \boldsymbol{\rho} \times \mathbf{G}_g(\mathbf{r}_0) dM \tag{22}$$

The total torque for the case of a spacecraft made by several parts, can be expressed as the sum of the torques given by the gravitational forces acting on each part i, hence resulting into:

$$\mathbf{T}_g = \sum_i \left(\int_{\text{i-th part}} \boldsymbol{\rho}_i \times \mathbf{a}_g(\mathbf{r}_i) dM_i \right) = \sum_i \left(\boldsymbol{\rho}_i \times \mathbf{a}_g(\mathbf{r}_i) M_i \right) \tag{23}$$

Where $\boldsymbol{\rho}_i$ is the position of a point of the i-th part with respect to the center of mass of the i-th part itself. As before, this method is both more precise and more expensive from the computational point of view.

D. Solar Radiation Pressure Forces Modeling

The exchange of momentum between the photons and a surface gives the solar radiation pressure. Each source of electromagnetic radiation has an effect on a solid surface, but the pressure given by the solar radiation is predominant at 1AU [46], thus the other terms are negligible in this analysis. In a Macro-Model approach, the incident radiation on a surface can be either absorbed, specularly reflected, and diffusely reflected (by assuming no transmission of radiation through the spacecraft). In the following, dA is the surface area with normal $\hat{\mathbf{n}}$ subjected to the incident flux Φ. The incident flux has an inclination α with respect to the normal $\hat{\mathbf{n}}$. The unit vector $\hat{\mathbf{s}}$ points towards the origin of the radiation. The summation of the three forces given by the absorption, the specular reflection, and the diffusive reflection of the incoming radiation gives the total resultant force over a flat surface dA.

$$d\mathbf{f}_p = d\mathbf{f}_{ps} + d\mathbf{f}_{pd} + d\mathbf{f}_{pa} = -\frac{\Phi}{c} dA cos\alpha \left[\left(2C_{ps} cos\alpha + \frac{2}{3} C_{pd} \right) \hat{\mathbf{n}} + \left(C_{pd} + C_{pa} \right) \hat{\mathbf{s}} \right] \tag{24}$$

1. Solar Radiation Pressure Forces and Torques

The two models suitable for the computation of the Solar Radiation Pressure effects are the Cannonball Model and the Backward Ray-Casting Model.

Cannonball Model

The cannonball model is a classical simplified approach to compute the resultant force over the external surfaces of a spacecraft. The spacecraft can be approximated by a sphere of equivalent external area and with constant thermo-optical properties as assumption of this model. The incoming flux of electromagnetic radiation is incident over the cross sectional area, thus the total force becomes:

$$\mathbf{f}_p = -\frac{\Phi}{c} \pi R^2 \left(C_{ps} + \frac{13}{9} C_{pd} + C_{pa} \right) \hat{\mathbf{s}} \tag{25}$$

with this model, the determination of the resulting torque is not possible (indeed $\mathbf{T}_p = 0$).

Backward Ray-Casting Model

This method relies on the generation of rays on the surfaces of the spacecraft. The propagation of these rays in the backward direction allows to check if there are intersections and shadowing between surfaces. The spacecraft surfaces must be approximated as an ensemble of large arrays made by small "facets" in order to apply this method. Each facet acts as a source for a single ray thus, if the facets are small enough, the total force can be computed as a summation instead of solving the integral over the entire surface. If $\hat{\mathbf{s}} \cdot \hat{\mathbf{n}} < 0$, the facet is certainly in shadow, hence the ray and the facet can be discarded immediately from the computation. A ray-casting intersection algorithm is needed to evaluate the rays that intercept one surface before reaching another one. The contribution must be discarded after

the first intersection. The degree of precision depends on the number of facets used. The higher the number of facets the higher the precision, but also the higher the computational cost. If thin-wires or, more in general, thin features are present, the aliasing may arise (as in the case of forward ray-casting), but the error introduced is usually not significant.

E. Electrostatic Force Modeling

To include the plasma wake effects is one of the biggest issues in modeling the electrostatic field, and all the analytical models seem to be inadequate for this purpose. For this reason, the electrostatic field and the electrostatic potential are external input data by the user. These externally given data represent the electrostatic field and potential sampled on a 3D Cartesian mesh of points. The data (both for the electrostatic potential and the electrostatic field) are given in RIC reference frame and they are time invariant [40] by assumption (see also Sec. III). The time-invariant nature of the data is a strong assumption, but otherwise, the implementation of a dynamic model for the data will result in a high computational load and, moreover, it will imply also the need for storage capabilities for a huge amount of data.

1. Electrostatic Forces and Torques

The computation of both the force $\mathbf{f}_e$ and the torque $\mathbf{T}_e$ exerted on the spacecraft is possible by starting from the input files containing the values of the electrostatic field for the asteroid and the plasma under analysis.

Electrostatic Forces

We can consider the spacecraft or as an extended body characterized by a net charge and first and second moment of charge, or as an ensemble of parts, each one characterized by a net charge localized in the center of charge of the part (which could be not coincident with the center of mass of the part itself). If the assumption of a unique extended body is valid for the spacecraft, the electric field is linear by assumption (as done for the gravity field in Sec. II.C), thus by defining $\boldsymbol{\rho}$ as previously done in Sec. II.C, the electric field can be expressed as:

$$\mathbf{E}(\mathbf{r}) = \mathbf{E}(\mathbf{r}_0) + \mathbf{G}_e(\mathbf{r}_0)\boldsymbol{\rho} \tag{26}$$

In which $\mathbf{G}_e(\mathbf{r}_0)$ is the electrostatic field gradient computed in the center of mass of the spacecraft. The derivation of an analytical expression is not possible for the electrostatic field gradient, thus it is numerically computed starting from the data of the electrostatic field. The tensor $\mathbf{G}_e(\mathbf{r}_0)$ is obtained by building a $3x3$ matrix in which each column is the vector of the gradient of the electrostatic field computed each time along one of the three directions. Hence the electrostatic force is:

$$\mathbf{f}_e = \int_{S/C} [\mathbf{E}(\mathbf{r}_0) + \mathbf{G}_e(\mathbf{r}_0)\boldsymbol{\rho}]\, dq = \mathbf{E}(\mathbf{r}_0) \int_{S/C} dq + \mathbf{G}_e(\mathbf{r}_0) \int_{S/C} \boldsymbol{\rho} dq = \mathbf{E}(\mathbf{r}_0)q + \mathbf{G}_e(\mathbf{r}_0)\mathbf{S}_q \tag{27}$$

The left integral cannot be canceled out because the center of charge may not coincide with the center of mass of the spacecraft. In analogy with the mass-related cases, this term is the first moment of charge $\mathbf{S}_q$ about the center of mass. This term is negligible if the center of mass and the center of charge are coincident. If the spacecraft is an ensemble of i-parts, the summation of the force acting on each part is the total force given by the electrostatic field. By naming $\mathbf{r}_i$ the position of the center of mass of each part, the total electrostatic force is:

$$\mathbf{f}_e = \sum_i \left(\int_{i-thpart} \mathbf{E}(\mathbf{r}_i) dq_i \right) = \sum_i \left(\mathbf{E}(\mathbf{r}_i) \int_{i-thpart} dq_i \right) = \sum_i (\mathbf{E}(\mathbf{r}_i) q_i) \tag{28}$$

As for the previous case, this method allows to achieve a higher accuracy (especially in those cases in which the spacecraft is highly distributed and thus the linear approximation is no longer valid) but has as drawback a higher computational cost.

Electrostatic Torques

The torque due to the electric field on an extended spacecraft with respect to the center of mass of the spacecraft itself is:

$$\mathbf{T}_e = \int_{S/C} \boldsymbol{\rho} \times \mathbf{E}(\mathbf{r}) dq \tag{29}$$

By considering the spacecraft as a single extended body, the linear approximation for the local variation of the electric field is valid, thus Eq. (29) can be rewritten as:

$$\mathbf{T}_e = \int_{S/C} \boldsymbol{\rho} \times [\mathbf{E}(\mathbf{r}_0) + \mathbf{G}_e(\mathbf{r}_0)\boldsymbol{\rho}] \, dq = \int_{S/C} \boldsymbol{\rho} dq \times \mathbf{E}(\mathbf{r}_0) + \int_{S/C} \boldsymbol{\rho} \times \mathbf{G}_e(\mathbf{r}_0)\boldsymbol{\rho} dq = \mathbf{S}_q \times \mathbf{E}(\mathbf{r}_0) + \mathbf{T}_{eG} \tag{30}$$

Where $\mathbf{T}_{eG}$ involves the computation of the second moment of charge $\mathbf{I}_q$, which is similar to the computation of the mass inertia tensor $\mathbf{J}$, with charges instead of masses. If the spacecraft is made of multiple parts, the transport theorem can be applied to translate all the contributions of each part to a reference point and then the summation of these contributions gives the second moment of charge of the entire spacecraft. $\mathbf{T}_{eG}$ can be computed as the gravitational torque, thus:

$$\mathbf{T}_{eG} = \begin{bmatrix} G_{e,yz}(I_{q,zz} - I_{q,yy}) + G_{e,xz}I_{q,xy} - G_{e,xy}I_{q,xz} + I_{q,yz}(G_{e,zz} - G_{e,yy}) \\ G_{e,xz}(I_{q,xx} - I_{q,zz}) - G_{e,yz}I_{q,xy} + G_{e,xy}I_{q,yz} + I_{q,xz}(G_{e,xx} - G_{e,zz}) \\ G_{e,xy}(I_{q,yy} - I_{q,xx}) + G_{e,yz}I_{q,xz} - G_{e,xz}I_{q,yz} + I_{q,xy}(G_{e,yy} - G_{e,xx}) \end{bmatrix} \tag{31}$$

With $\mathbf{G}_e(\mathbf{r}_0)$ computed at the center of mass. If the spacecraft is an ensemble of parts by assumption, the total torque

acting on the spacecraft is the summation of the torques generated by the electrostatic field on each part i. By calling $\mathbf{r}_i$ the position of the center of mass of the *i-th* part, Eq. (29) becomes:

$$\mathbf{T}_e = \sum_i (\boldsymbol{\rho}_i \times \mathbf{E}(\mathbf{r}_i) q_i) \tag{32}$$

This last formulation offers a more accurate estimation of the torque given by the electrostatic field, but the computational load is higher, as in the previous cases.

III. Plasma Interaction and Charging

The collision mean-free-path in the solar wind is typically on the order of one to tens of Km. Hence, for small asteroids (i.e. size smaller than 1 Km), the solar wind plasma flow around asteroid can be considered collisionless [4, 22]. The collisionless nature of plasma flow around small asteroids renders the PIC simulation method, which solves plasma particle trajectory, space charge, and the Poisson equation self-consistently, as the preferred modeling method for solar wind-asteroid interactions.

In this paper, a 3D fully kinetic immersed-finite-element particle-in-cell model, USC-IFEPIC, [4, 22, 29, 47] is applied to obtain the plasma environment and the electric field around a small asteroid. The USC-IFEPIC model is a 3-D full particle electrostatic PIC code designed to simulate plasma interactions with arbitrarily shaped dielectric objects. In order to resolve the electron dynamics and the photoelectron sheath correctly, all plasma species (solar wind protons and electrons, photoelectrons, and secondary) are represented by macro-particles. The electric potential Φ, the space charge, and the trajectories of each macro-particle are solved self-consistently from the Poisson's equation and the Newton's second law:

$$\nabla \cdot (\epsilon_0 \nabla \Phi) = -e(n_i - n_e - n_{ph} - n_{se}), \;\; m\frac{d\vec{v}}{dt} = q(\vec{E} + \vec{v} \times \vec{B}) \tag{33}$$

Where n_i, n_e, n_{ph}, and n_{se} are the number densities of solar wind ion, solar wind electron, photoelectron, and secondary electron, respectively. In this paper, the contribution of secondary electrons emitted from the asteroid surface is ignored because the secondary density is orders of magnitude smaller than that of the other species [4, 18, 19]. In the simulation, an asteroid is considered as part of the simulation domain with dielectric properties explicitly included. The electric field is solved both inside and outside of the asteroid. The charging potential of the asteroid is calculated directly from charge deposition at the asteroid surface. The USC-IFEPIC model was validated against the 1D analytical solutions of [20, 26] in Ref. [4], and was previously applied to simulate lunar surface charging [47], asteroid charging [22], and charged dust dynamics around small asteroids [39].

Asteroids have a wide range in size and many different shapes, and the solar wind plasma can undergo substantial changes. In this paper, for simplicity, we consider a spherical asteroid with a radius of $r_a = 14\ m$ and a relative

permittivity of $\epsilon_r = 4$ under the average solar wind plasma condition at 1 AU. The asteroid size considered is similar to that of the near-Earth asteroids 1998 KY26, 2004 FH, 367943 Duende, and 2014 RC, and the relative permittivity used is similar to that of the lunar regolith [39].

The average solar wind plasma parameters at 1AU are: plasma density $n_0 \simeq 5.6\ cm^{-3}$; solar wind flow speed $V_{sw} \simeq 400\ km/s$; solar wind electron temperature $T_e \simeq 15\ eV$, and solar wind ion temperature $T_i \simeq 10\ eV$. The photoelectron current under normal sunlight incidence at 1 AU is $I_{ph0} \simeq 4.5\ \mu A/m^2$ and the photoelectron temperature is $T_{ph} \simeq 2.2\ eV$. Hence, the number density of the photoelectron at asteroid surface as a function of the local sun elevation angle α is [48]:

$$n_{ph}(\alpha) \simeq 64 \sin(\alpha)\ cm^{-3} \tag{34}$$

For photoelectron emission at a sunlit surface under normal incidence, the photoelectron density at surface is $n_{ph0} \sim 64\ cm^{-3}$. Based on these parameters, the solar wind Debye length is $\lambda_{D0} \simeq 12\ m$. Under normal incidence of the sunlight, the photoelectron Debye length is $\lambda_{Dph0} \simeq 1.4\ m$. For surfaces with small sun incidence angles, the photoelectron Debye length would be significantly larger due to reduced photoelectron emission.

PIC simulations were first carried out to study the plasma environment around an asteroid and the asteroid charging process. Fig. 5 shows the electric potential contours. Taking advantage of the axial symmetry, the simulation domain contains only a quarter of the asteroid. The simulation domain has a size of $120 \times 30 \times 30$ PIC cells with a mesh resolution of $dx = dy = dz = \lambda_{Dph0} \simeq 1.4\ m$. Both the solar wind flow and the sunlight are taken to be along the x direction. In the simulation domain, the asteroid center is located at $(x, y, z) = (56\ m, 0, 0)$.

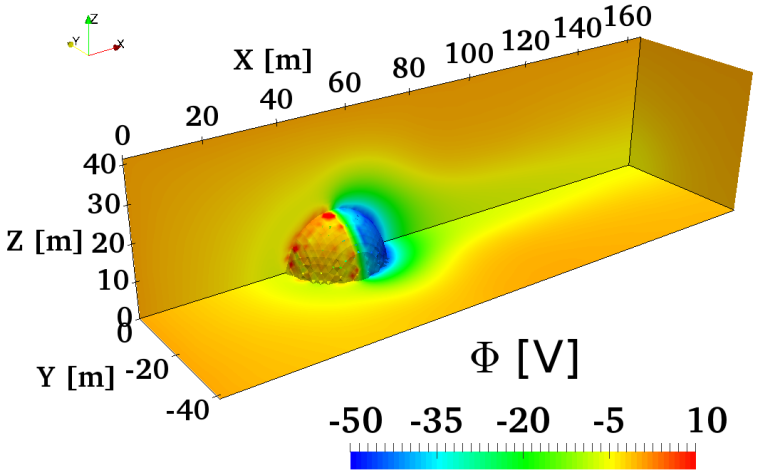

Fig. 5 IFEPIC Electric potential distribution around a small asteroid

Macro-particles representing solar wind electrons and ions are injected at each time step at the x = 0 boundary, following a drifting Maxwellian velocity distribution. Macro-particles representing the photoelectrons are emitted from the illuminated asteroid surface at each PIC time step as a stationary, half-Maxwellian velocity distribution. The real proton-to-electron mass ratio of $m_i/m_e = 1836$ is used so the correct mesothermal velocity ratio between the ions and electrons are preserved. The simulation is run on electron plasma time scale. At steady state, the number of macro-particles in the simulation domain is on the order of 10^7. For the solar wind plasma and photoelectron parameters considered here, the asteroid surface potential with respect to the ambient plasma ranges from about $\Phi_a \sim +9\ V$ on the sunlit surface to $\Phi_a \sim -43\ V$ on the shadowed surface. The photoelectron sheath on the ram side and the plasma wake region are evident in Fig. 5.

PIC simulations were then carried out to include an E-Glider hovering at selected locations above the asteroid. The potential of the E-Glider is determined by the E-Glider's capacitance and the charging mechanism utilized. Within the scope of this paper, we do not invoke a specific E-Glider electrode design and charging mechanism. Hence, in this simulation, we assume that the E-Glider is at the naturally occurring floating potential as determined self-consistently by current collection in plasma.

Figure 6 shows the electric potential contours for an E-Glider hovering at a height of about 10 m above the asteroid on the terminator line. Here, the simulation parameters are the same as that in Fig. 5. The E-Glider is modeled as a 1-cell-sized conducting cube. The potential of the E-Glider obtained from the PIC simulation is found to be $\Phi_s \simeq -3.7\ V$.

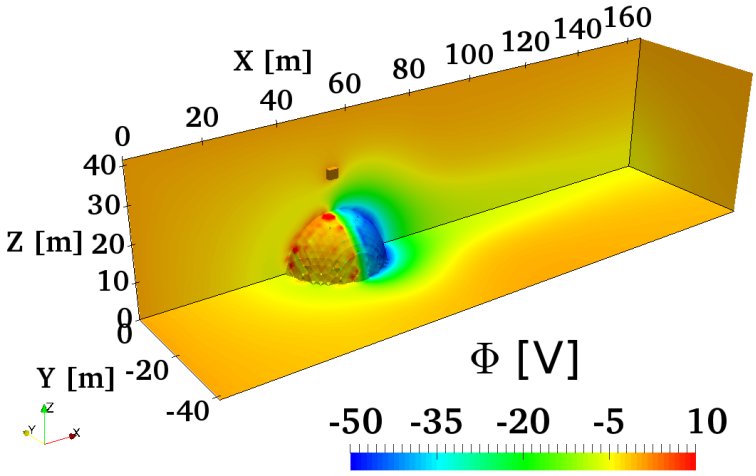

Fig. 6 IFEPIC Electric potential distribution around a small asteroid with a spacecraft at floating potential hovering at 10m above the asteroid

Figure 6 shows that, at the floating potential, the perturbation of the E-Glider on the plasma environment and on the electric field generated by the asteroid is not significant. This conclusion is generally true for naturally charged spacecraft in the average solar wind plasma environment at hovering locations around the asteroid considered here [49].

We note that the E-Glider potential could be significantly higher than that in Figure 6 if the spacecraft was in a severely charging plasma environment or was charged by artificial means. At a sufficiently high potential, the spacecraft sheath can overlap with that of the asteroid and thus the E-Glider can interact directly with asteroid as well as with plasma. This is the multibody-plasma interaction (MPI) interaction [50]. At the floating potential, the electrostatic force between E-Glider and asteroid is at the weakest for a given amount of net charge due to shielding by plasma sheath. On the other hand, under the MPI situation, the effects of plasma shielding will be at the minimum and the electrostatic force starts to approach the Coulomb force in vacuum, thus creating a more favorable condition for electrostatic hovering.

As it is not computationally feasible to carry out PIC simulations for every case involved in the dynamics analysis of the E-Glider, in the rest of the paper, we will assume that the E-Glider is charged to the floating potential determined by the average solar wind condition and we will ignore the perturbation of the E-Gilder on the electric field generated by the asteroid. The electrostatic force on the E-Glider will be estimated as defined in Sec. II.E, where the electric field data are obtained from the PIC simulations presented above.

IV. Electrostatic Hovering

Hovering is a type of active control in which a continuous control thrust cancels out the nominal accelerations acting on the spacecraft [51, 52]. For the E-Glider, the net charge Q of the spacecraft itself generates the thrust or better, a continuous force. The solar radiation pressure has a strong influence on the shape of the orbits near a small body like an asteroid (leading also to the instability in some cases [11]), due to the weak gravitational attraction. For this reason, the Solar Radiation Pressure (SRP) effects are included in the analyses. The hovering can be a solution to avoid these problems by eliminating the disturbance accelerations of the spacecraft through an active control, thus creating an artificial equilibrium point at a desired location. Until now, fuel restrictions limited the hovering applications, but for the E-Glider these limitations do not apply, since only physical or technological constraints on the power consumption and on the potential reached by the electrodes of the spacecraft will set a limit and not the fuel level. Before approaching the hovering problem, we analyzed the zero-velocity curves to better understand the potential field near the asteroid. The equations of motion contain the electrostatic potential term in order to make this analysis relevant to the E-Glider case. The analysis points out that the previously used Nitter model turned out not to be adequate to describe the electrostatic field in close proximity of an asteroid since, by using the more refined model provided by the PIC analysis, the identification of new and more equilibrium points with respect to the ones predicted by the Nitter model is possible. This led also to the possibility of identifying stable equilibrium points in the subsolar hovering conditions on the sunlit side, which are at an altitude of about $10 - 100$ meters from the surface of the asteroid. An E-Glider can hover at these

points by using a charge level lower than the one predicted by using the Nitter model. The sensitivity analysis shows that the charge over mass ratio needed to hover grows quadratically with the radius of the spacecraft.

Assumptions

This paragraph summarizes the assumptions used to define the case study and under which the obtained results are valid. The bodies in the system under investigation are the Sun, a reference asteroid (considered as the Main Body) in a heliocentric orbit, and a Spacecraft orbiting in close proximity of the asteroid. The Main Body has a circular heliocentric orbit by assumption, thus the equations of motion can be written by using the Clohessy-Wiltshire approximation [41].

Spacecraft Properties

We assumed the spacecraft to be a solid sphere, to include the extended SRP effects. The mass of the spacecraft is constant and equal to 1.33 Kg (as for a 1U CubeSat*). The radius of the reference spacecraft is equal to 0.065 m (it is computed from the volume of a sphere equivalent to a 1U CubeSat). The computation of the SRP properties of the spacecraft can be performed by assuming a layer of Mylar with a coefficient of absorptance (C_{pa}) equal to 0.14 [53] that covers the surface. The coefficients of specular (C_{ps}) and diffuse (C_{pd}) reflection have the same value, equal to 0.43, by assumption. The SRP force is modeled by using the backward ray-casting model. The charge Q is considered to be fixed and modeled as a point charge concentrated in the center of mass of the spacecraft, thus the first moment of charge is zero. Table 1 summarizes the spacecraft characteristics.

Table 1 Reference Spacecraft Characteristics

Parameter	Value
Shape	Sphere
Radius	0.065 m
Mass	1.33 Kg
C_{pa}	0.14
C_{ps}	0.43
C_{pd}	0.43

Main Body Properties

The Main Body used in these simulations is the reference asteroid used also for the PIC (Particle-In-Cell) analysis [39] from which the plasma data are given. The reference main body is a spherical asteroid with radius 14 m. The gravity model used is the Point Mass model with $\mu = 0.0017\ m^3/s^2$. The circular heliocentric orbit of the asteroid has radius 1AU and period of 365.25 days at epoch 2451545 JD. The rotational parameters are assumed to be measured at the same epoch of the orbital parameter. The right ascension of the rotational axis is set to 0 deg and the declination to 90

*NASA, CubeSats Overview, `https://www.nasa.gov/mission_pages/cubesats/overview`, Accessed: 03-10-2019

deg with a rotational period of 1 deg/day. Table 2 summarizes the orbital and the rotational parameters of the asteroid.

Table 2 Reference Asteroid Characteristics

Orbital Parameters		**Rotational Parameters**	
Epoch	2451545 JD	Epoch	2451545 JD
Epoch Offset	0	Epoch Offset	0
Mean Anomaly	0	Rotational Axis RA	0
Orbital Period	365.25 days	Rotational Axis DE	90 deg
Semimajor Axis	1 AU	Prime Meridian Position	0
Eccentricity	0	Rotational Period	1 deg/day
Inclination	0	**Geometry**	
RA of Ascending Node	0	Shape	Sphere
Argument of Periapsis	0	Radius	14 m
Gravity		**Plasma**	
Gravity Model	Point Mass	Plasma Field	True
Gravitational Parameter	$0.0017\ m^3/s^2$		

A. Zero Velocity Curves

Mathematical Derivation

The Clohessy-Wiltshire equations derived in Sec. II.B.1 (see Eq.(9) and Eq. (10)) can be re-written in RIC frame as [41]:

$$\begin{aligned} \ddot{x} - 2N\dot{y} &= -\frac{\partial U}{\partial x} \\ \ddot{y} + 2N\dot{x} &= -\frac{\partial U}{\partial y} \\ \ddot{z} &= -\frac{\partial U}{\partial z} \end{aligned} \tag{35}$$

In Eq. (35), U is the potential as a function of the position of the spacecraft $\mathbf{r}$. For the case under analysis, the contributions to the total potential are the gravitational effect, the centrifugal effect and the equivalent potential given by the solar radiation pressure and by the electrostatic potential. Thus:

$$\begin{aligned} -\frac{\partial U}{\partial x} &= 3N^2 x + a_{g,x} + a_{p,x} + \frac{Q}{M}E_x \\ -\frac{\partial U}{\partial y} &= a_{g,y} + a_{p,y} + \frac{Q}{M}E_y \\ -\frac{\partial U}{\partial z} &= -N^2 z + a_{g,z} + a_{p,z} + \frac{Q}{M}E_z \end{aligned} \tag{36}$$

By integrating and by assuming a simplified case in which the potential of the SRP force is $U_p = \mathbf{a}_p \cdot \mathbf{r}$ as in [10],

the potential can be written as:

$$U(\mathbf{r}) = -U_g(\mathbf{r}) - \frac{N^2}{2}\left(3x^2 - z^2\right) + \frac{Q}{M}\phi_e(\mathbf{r}) - \mathbf{a}_p \cdot \mathbf{r} \tag{37}$$

Where $U_g(\mathbf{r})$ is the gravitational potential (resulting from the integral of $\mathbf{a}_g = \nabla U_g$) and $\phi_e(\mathbf{r})$ is the electrostatic potential in $\mathbf{r}$ resulting from the integral of $\mathbf{E} = -\nabla\phi_e$. Equation (35) can be written in a more compact form:

$$\frac{\partial^2 \mathbf{r}}{\partial t^2} = -\nabla U \tag{38}$$

But:

$$\frac{\partial \mathbf{r}}{\partial t} \cdot \frac{\partial^2 \mathbf{r}}{\partial t^2} = -\frac{\partial \mathbf{r}}{\partial t} \cdot \nabla U \tag{39}$$

Where:

$$\frac{\partial \mathbf{r}}{\partial t} \cdot \frac{\partial^2 \mathbf{r}}{\partial t^2} = \mathbf{v} \cdot \dot{\mathbf{v}} = \frac{1}{2}\frac{d^2}{dt}v^2 \tag{40}$$

Where $\mathbf{v}$ and $\dot{\mathbf{v}}$ are computed relative to the co-moving frame. Moreover, we observe that:

$$\frac{\partial \mathbf{r}}{\partial t} \cdot \nabla U = \frac{\partial \mathbf{r}}{\partial t}\nabla U^T = \frac{\partial U}{\partial x}\frac{\partial x}{\partial t} + \frac{\partial U}{\partial y}\frac{\partial y}{\partial t} + \frac{\partial U}{\partial z}\frac{\partial z}{\partial t} = \frac{dU}{dt} \tag{41}$$

Thus:

$$\frac{1}{2}\frac{d}{dt}v^2 = -\frac{dU}{dt} \Rightarrow \frac{1}{2}\frac{d}{dt}v^2 + \frac{dU}{dt} = 0 \Rightarrow \frac{d}{dt}(v^2 + 2U) = 0 \tag{42}$$

This led to $v^2 + 2U \doteq C_j$ which is constant and corresponds to an Integral of Motion (or the Jacobi Integral). The total energy can be written as $\frac{1}{2}v^2 + U = E_{TOT}$. Since $v^2 \geq 0$ is always true, $U(\mathbf{r}) \leq C_j$ must hold. This last equation defines a constraint for the allowable regions for the spacecraft. The boundaries of these regions are the zero-velocity curves. The potential $U(\mathbf{r})$ is affected by the spacecraft charge Q (see Eq. (37)), thus an analysis for different levels of Q in proximity of the asteroid allows to better understand the presence of equilibrium points and the U-transitions. The equilibrium points can be obtained by imposing $\frac{d}{dt} = 0$ in Eq.(35), resulting in the equilibrium conditions $\frac{\partial U}{\partial x} = \frac{\partial U}{\partial y} = \frac{\partial U}{\partial z} = 0$. The analysis here presented are reduced to the *xy-plane* in which the negative x is the sunlit side of the asteroid, with the sunlight coming from -x direction.

Case 1: $Q = 0\ \mu C$

Here, the case for $Q = 0\mu C$ is analyzed. The results obtained and showed in Fig. 7 are consistent with the ones already presented in [28]. Only one equilibrium point exists in proximity of the asteroid on the dark side. In the equilibrium point, the effect of the SRP plus the centrifugal force (both acting in +x-direction) counter the effect of the gravitational acceleration of the asteroid. The potential is negative, with negative peaks in proximity of the planet.

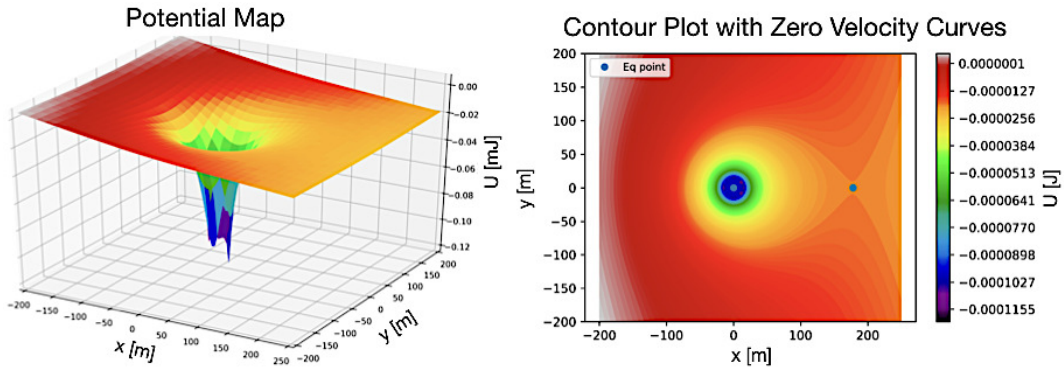

Fig. 7 Potential Map and Zero Velocity Curves for Q = 0μC

Case 2: $Q > 0\ \mu C$

When the spacecraft has a positive charge, the influence of the charge itself on the potential field is not strong. On average, if the positive charge is increased, the potential field is "pushed" through more negative values. The main behavior in close proximity of the asteroid is not strongly affected by the charge as the potential keeps decreasing through highly negative values as in the case for $Q = 0$. Figure 8 shows the zero velocity curves plotted for the cases of $Q = 15\mu C$ (top), $Q = 25\mu C$ (mid) and $Q = 75\mu C$ (bottom).

The blue dots are the equilibrium positions. The plots on the right column of Fig. 8 are the details of the plots on the left column computed only for the sunlit region ($-55 \leq x \leq 0$ and $0 \leq y \leq 40$) with a more refined mesh. By looking first at the plots on the left column, we can notice that different levels of positive charge do not have a strong impact on the shape of the potential field. Moreover, the effects of the plasma wake are evident (obviously they are not present if $Q = 0$, see Fig. 7). The modifications in the potential field given by the influence of the plasma are different from the results previously obtained by using the Nitter model [28], especially in the terminator line (transition between sunlit side and dark side) and in close proximity of the asteroid surface. By neglecting the non-feasible equilibrium point located at $x = y = z = 0$, there is at least one collinear ($y = 0$) equilibrium position on the dark side, far from the surface at about $105 - 110$ meters. These equilibrium points disappear (as shown in Fig. 8 for $Q = 75\mu C$) if the level of charge reaches high values, in this case, higher than $50\mu C$. Due to the presence of a photoelectron sheath near the surface of the asteroid, the presence of equilibrium points can be hypothesized for a positively charged spacecraft in this region. To detect these points, we needed an extremely refined mesh, for this reason, the plots on the right column of

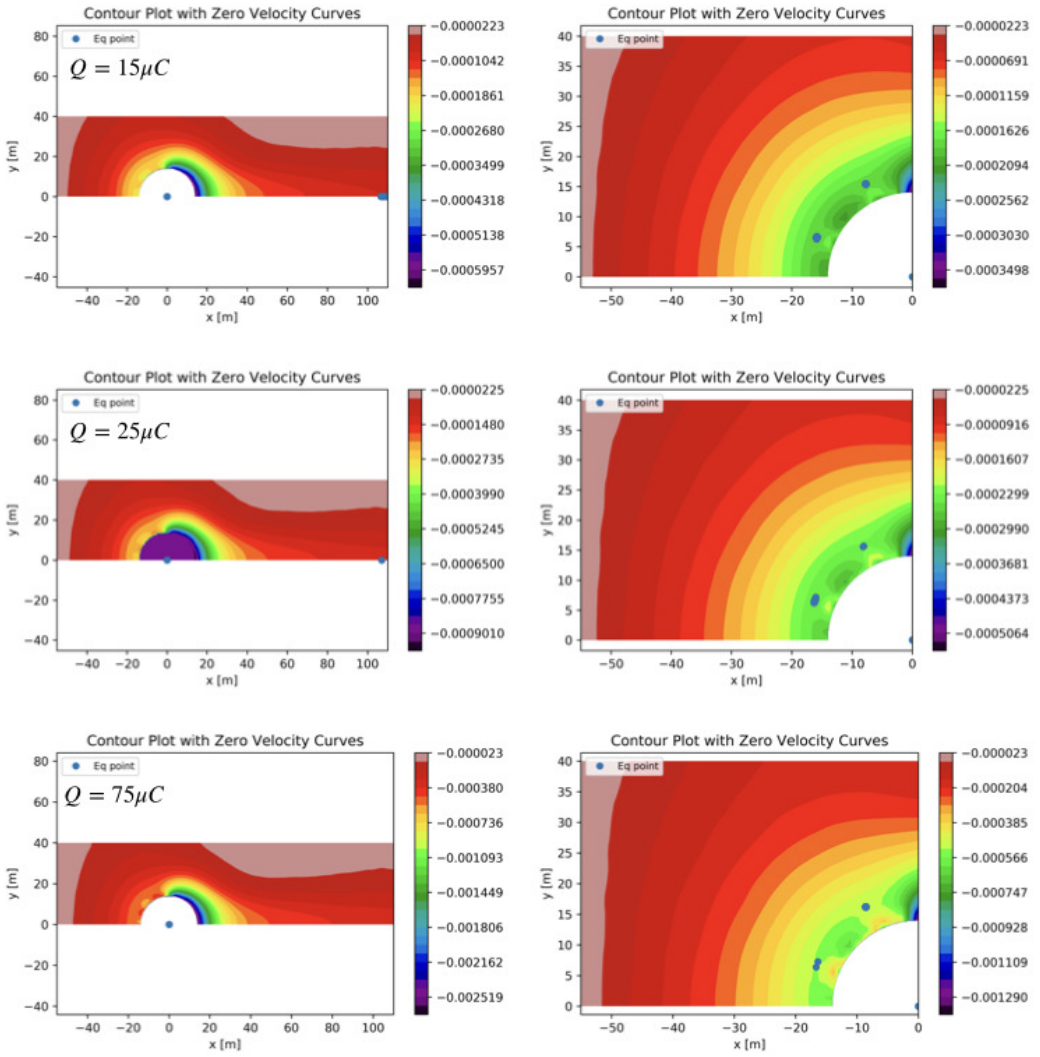

Fig. 8 Zero Velocity Curves for Q > 0μC

Fig. 8 were produced. These analyses indicated the presence of more equilibrium points. These new equilibrium points are non-collinear (they have $y \neq 0$) and, moreover, there are more-than-one non-collinear equilibrium points for the same level of charge Q. This result is the consequence of the complex shape of the electric field near the surface of the asteroid. These points were not detectable with the Nitter model, since it uses an oversimplified model for the electric field computation with respect to the PIC results. The mesh used does not allow to find collinear equilibria in the sunlit side, but their presence can be predicted by considering again the photoelectron sheath. The mesh must be excessively fine to detect these points, leading to a strong increment in the computational time. The analyses restricted to the case of $y = z = 0$ and $x \neq 0$ reported in the following sections confirm the presence of these equilibrium points at an altitude below ≈ 2 meters (altitude at which the electrostatic potential has a minimum, thus an inversion of the sign in E_x), but with a strong gradient of variation of Q for small variation in the position x. The non-collinear points obtained are not

very sensitive to variations in the charge levels, furthermore, they are still present even for levels of charge in which the dark side equilibrium point has already disappeared. The coexistence (at least for a low positive charge) of equilibrium points both on the sunlit side and on the dark side is ensured, with both collinear and non-collinear points on the sunlit side.

Case 3: $Q < 0\ \mu C$

In this case, the spacecraft has a negative charge. The charge of the spacecraft affects the potential field in a way that on the sunlit side the potential falls to extremely negative values, while on the dark side the potential becomes strongly positive in close proximity of the surface. Figure 9 shows the zero velocity curves plotted for the cases of $Q = -5\mu C$ (left) and $Q = -10\mu C$ (right).

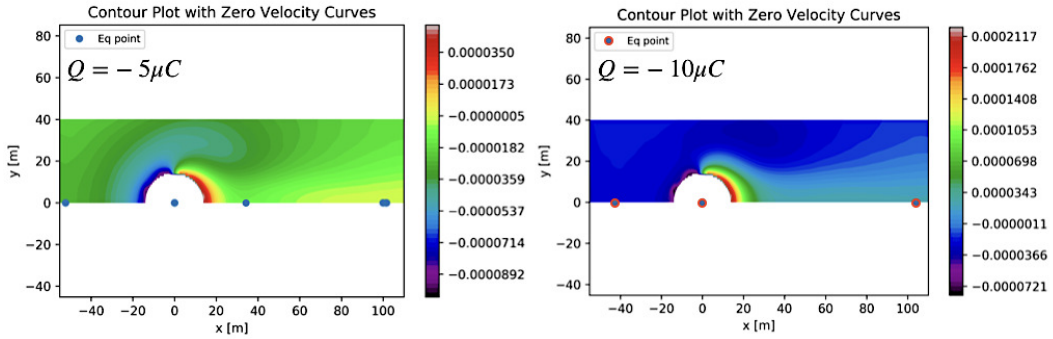

Fig. 9 Zero Velocity Curves for Q < 0μC

The equilibrium conditions are present both on the sunlit side and on the dark side, even for a low level of charge. Moreover, there is more than one equilibrium condition on the same side for the same level of charge. This result is in contrast with the previous study [28] based on the Nitter model. By using the Nitter model the equilibrium conditions were obtained only on one side per time with a negatively charged spacecraft, moreover, the equilibrium conditions on the sunlit side were obtained only for extremely high levels of charge [28]. A comparison between the equilibrium points on the sunlit side for the two cases reported indicated that the equilibrium points are closer to the asteroid surface for a charge higher in modulus. Also, this result is in contrast with the Nitter theory, where an increasingly negative charge moves the spacecraft far away from the asteroid towards the Sun direction [28]. The detection of equilibrium positions on the sunlit side is affected by the dimensions of the mesh, thus also in this case in order to augment the number of points in the grid without strongly affecting the computational time, some analyses have been performed for the case in which $-55 \leq x \leq 0$ and $0 \leq y \leq 40$ with a more refined mesh. The results are in Fig. 10.

There are more equilibrium positions, for the same level of charge, on the subsolar axis, as deduced before. Moreover, several non-collinear equilibrium points (equilibrium points with both x and y different from zero) are present also for a low level of charge. A comparison between the three cases reported in Fig. 10 indicated a drift of the equilibrium points

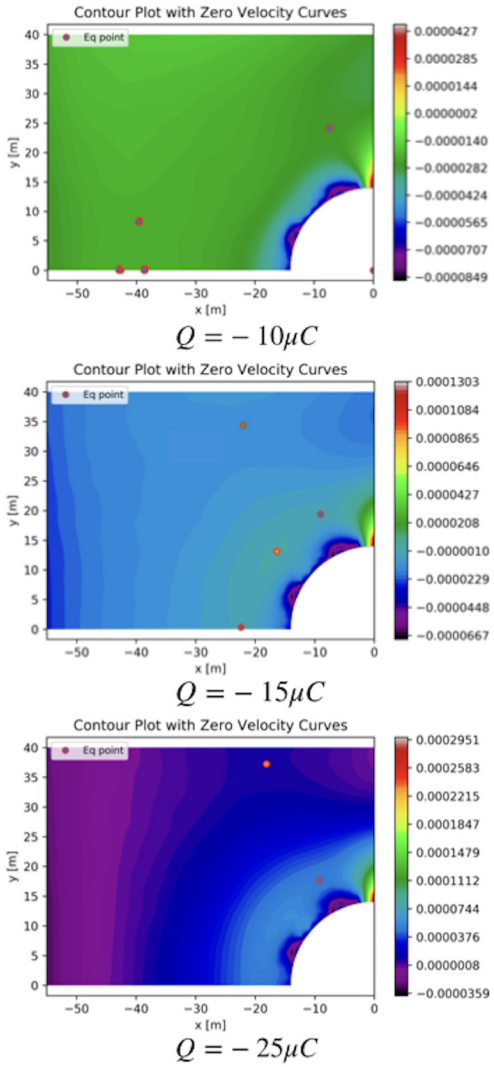

Fig. 10 Zero Velocity Curves for Q < 0μC on sunlit side

for different levels of charge. By making the charge more negative the collinear equilibrium points move towards the surface of the asteroid until they disappear (see the case of $Q = -25\mu C$), while the non-collinear points seem to drift away and some of them seem to appear and then disappear (a better understanding of this phenomenon can be obtained by using an extremely refined mesh). These results can not be obtained by using the Nitter model. Specifically, we note that the presence of more than one non-collinear equilibrium position has not been assessed before.

B. Subsolar Hovering

The analysis of the zero velocity curves points out that there are several equilibrium points dependent on the charge. The analysis was restricted to only the subsolar axis (thus only along the x-direction, with $y = 0$ and $z = 0$) in order to better characterize the equilibrium conditions in this region by achieving a higher accuracy without strongly refining the mesh. The equation for the hovering along the x-axis (Eq. (43)) can be derived from the general equation of motion

written under the Clohessy-Wiltshire assumptions, thus:

$$3N^2 x + \frac{f_{g,x}}{M} + \frac{f_{p,x}}{M} + E_x \frac{Q}{M} = 0 \tag{43}$$

The solution of Eq. (43) for Q/M gives the charge over mass ratio needed to hover at each position along the x-axis. The stability has been evaluated for each equilibrium condition. The stability conditions for the case under consideration are:

$$\frac{\partial U}{\partial x} = 0 \tag{44}$$

$$\left.\frac{\partial^2 U}{\partial x^2}\right|_{eq} > 0 \tag{45}$$

Where the selected Q/M verifies always Eq. (44). The x-derivative of Eq. (43) leads to:

$$\frac{\partial^2 U}{\partial x^2} = -3N^2 - \frac{\partial^2 U_g}{\partial x^2} - \frac{\partial a_p}{\partial x} - \frac{Q}{M}\frac{\partial E_x}{\partial x} \tag{46}$$

The second derivative of the gravitational potential is computed by using the Pines' algorithm with a modified recursion formula [42, 43, 45, 54]. The derivative of the electric field can be numerically computed as the x-component of the gradient of the electrostatic field. The term $\frac{\partial a_p}{\partial x}$ can be neglected since the E-Glider is supposed to orbit in close proximity to the asteroid, thus $\frac{\partial a_p}{\partial x} \approx 0$ can be assumed. The results of this first analysis are shown in Fig. 11.

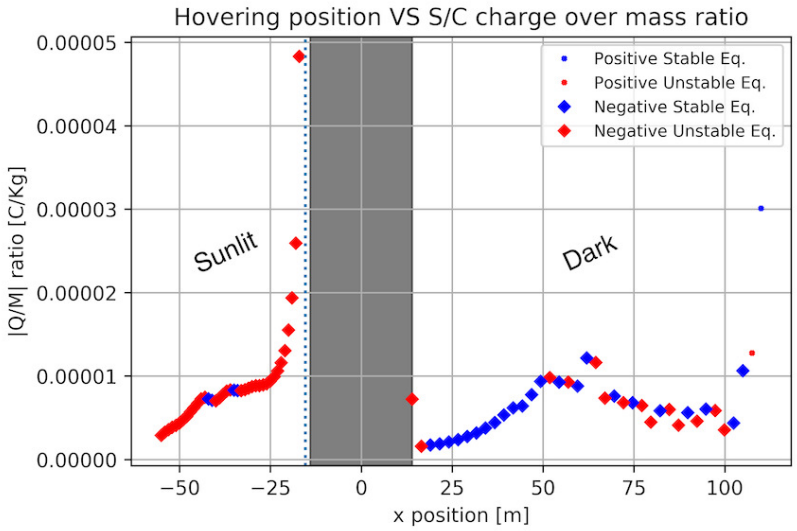

Fig. 11 Subsolar Hovering Conditions

The central grey band in Fig. 11 represents the asteroid and the blue-dotted line represents the limit of the nominal photoelectron sheath (which corresponds to the nominal photoelectron Debye length, equal to 1.38 m). Only a few

points of stable hovering over the sunlit face exist. These points are at about 42 meters from the center of the asteroid and they can be interesting from a "real mission" point of view. A negatively charged spacecraft could achieve almost all the hovering conditions, except some positions on the dark side (at more than 100 meters of distance from the center of the asteroid) and for altitudes below the photoelectron sheath (which are not reported in the figure for scale issues, since these points are located at values even equal to $Q/M = 0.0024\ C/Kg$). This analysis, in agreement with the results obtained in [40], confirmed that in the nominal case, for the assumed spacecraft and main body parameters, the Q/M ratio required for the hovering over the sunlit face is of the order of $10^{-5}\ C/Kg$. A stable hovering at about $10 - 100$ meters altitude is possible by assuming that the levels of power and voltage required are achievable. Moreover, the level of charge needed to achieve the hovering condition in subsolar positions is lower than the one predicted by using the Nitter model [28].

Hovering Sensitivity to Radius

A sensitivity analysis of the equilibrium conditions has been performed by changing the value of the equivalent radius of the sphere which represents the spacecraft in order to improve the characterization of the hovering conditions. The values used for the simulations are summarized in Table 3.

Table 3 Radius values for simulations

Reference [m]	**Values [m]**								
0.065	0.1	0.25	0.5	0.75	1.0	2.0	5.0	7.5	10

The reference value is equal to the radius used for the previous analysis. The other parameters are kept fixed, thus only the radius changes. An analytical study has been performed before the numerical analysis. The Q/M equation can be written as:

$$\frac{Q}{M} = \left[-3N^2 x - \frac{f_{g,x}}{M} - \frac{f_{p,x}}{M}\right] \frac{1}{E_x} \tag{47}$$

By considering the spacecraft as a "point" concentrated in the center of mass of the equivalent sphere, the only term dependent from the radius of the sphere R_{SC} is the SRP force. By using the simple cannonball model (only for the analytical formulation), the derivative of Eq. (47) with respect to R_{SC} is:

$$\begin{aligned} \frac{\partial Q/M}{\partial R_{SC}} &= \frac{\partial}{\partial R_{SC}} \left(\frac{\Phi}{c}\pi R_{SC}^2 \left(C_{ps} + \frac{13}{9}C_{pd} + C_{pa}\right)\hat{\mathbf{s}}\right) \\ &= \frac{\Phi}{c}\pi 2 R_{SC} \left(C_{ps} + \frac{13}{9}C_{pd} + C_{pa}\right)\hat{\mathbf{s}} \end{aligned} \tag{48}$$

$\frac{\partial Q/M}{\partial R_{SC}}$ is linearly increasing for positive values of R_{SC}, thus the Q/M needed for the hovering in proximity of an

asteroid increases quadratically with the increment of the equivalent radius of the spacecraft (the minimum is achieved for $R_{SC} = 0$ which is a non feasible solution). The numerical results are shown in Fig. 12.

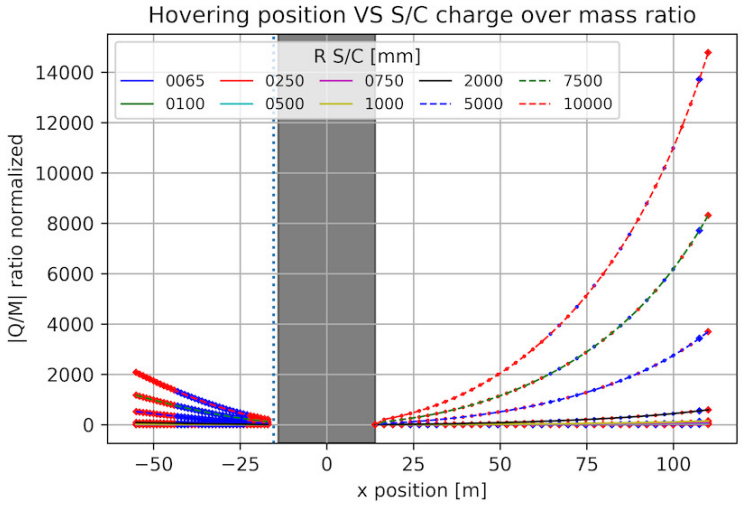

Fig. 12 Variation of normalized |Q/M| as function of R_{SC}

The big red marks represent unstable equilibrium positions achievable with a negative spacecraft charge, while the big blue marks represent the stable equilibrium positions obtained with a negative charge. The small markers represent equilibrium conditions achieved with positive charges (the color code for stable and unstable equilibria is the same). The simplified analytical approach is consistent with the numerical results. The Q/M needed to achieve the hovering condition increases with a quadratic law with the radius of the spacecraft. The Q/M ratios reported in Fig. 12 are the absolute value of the ones computed with a prefixed radius in a defined position normalized by the Q/M ratio obtained at the very same position for the reference radius. The normalized $|Q/M|$ increases both on the sunlit side and on the dark side by moving away from the surface. The variation of the spacecraft radius does not affect the stable equilibrium region. Figure 13 shows that on the dark side the behavior seems to be quite different from the predicted one.

The behavior of these curves is due to the fact that the normalized $|Q/M|$ is computed as the ratio between two absolute values. If the radius of the spacecraft increases, the transition from a negative to a positive Q/M ratio (obviously the sign is dictated by the charge Q) is anticipated; for $R_{SC} = 0.065$ the transition happens at ≈ 105 meters while for $R_{SC} = 0.5$ meters the transition happens at about 25 meters from the center of the asteroid, as it can be seen in Fig. 14. For a radius higher than 1 meter, the Q/M needed for the hovering on the dark side is positive for regions close to the asteroid. A second transition region located at about 105 meters can be identified in Fig. 14. This is due to the Electric field x-component that becomes positive.

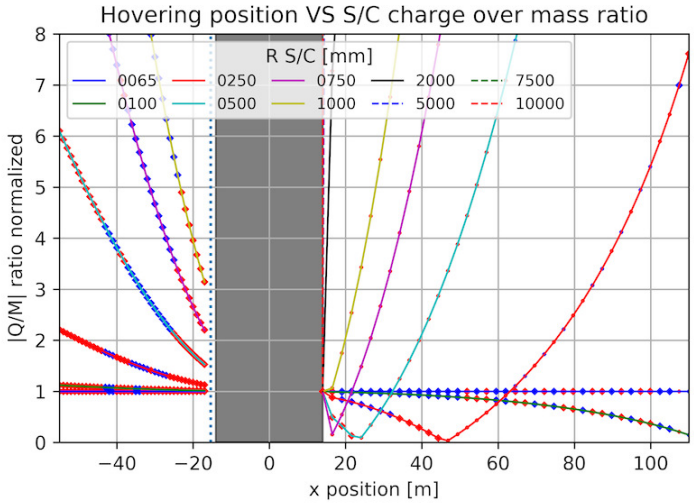

Fig. 13 Detail of Fig. 12

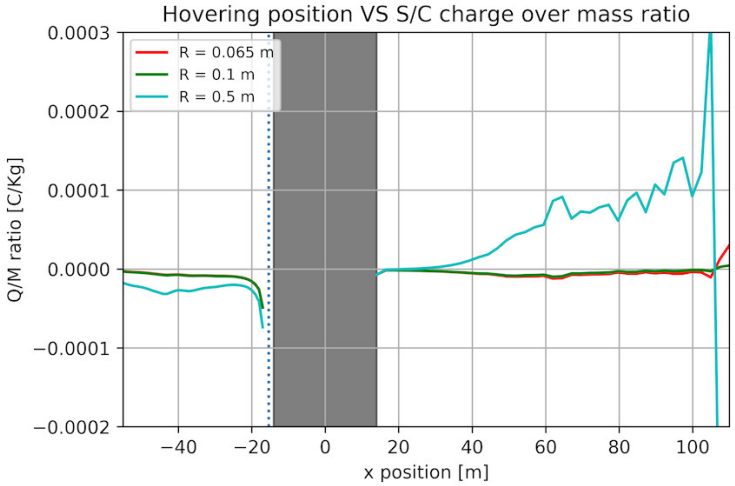

Fig. 14 Q/M for the first three cases examined

Hovering Sensitivity to Main Body Position

A sensitivity analysis to evaluate the effects of the position of the Main Body with respect to the Sun on the $|Q/M|$ ratio has been performed. The five different positions reported in Table 4 are considered in this analysis.

The positions considered are selected by considering the regions interesting for possible applications of an E-Glider. The case of an asteroid at 1AU is the reference for the analysis. By changing the distance with respect to the planet, the orbital period (computed in agreement with the selected semimajor axis) and the plasma parameters (the solar wind density and the solar wind ions and electrons temperature) change [18]. The variation of the plasma parameters strongly affects the current collected by the electrodes and the power needed to maintain the charge, but these effects are not considered in this analysis. The results of the numerical analysis are available in Fig. 15.

Table 4 Main Body Positions

Position [AU]	Reason
0.4	Mercury Orbit
1.0	Earth Orbit
1.5	Mars Orbit
2.2	Inner Asteroid Belt Radius
2.75	Mid Asteroid Belt Radius
3.3	Outer Asteroid Belt Radius

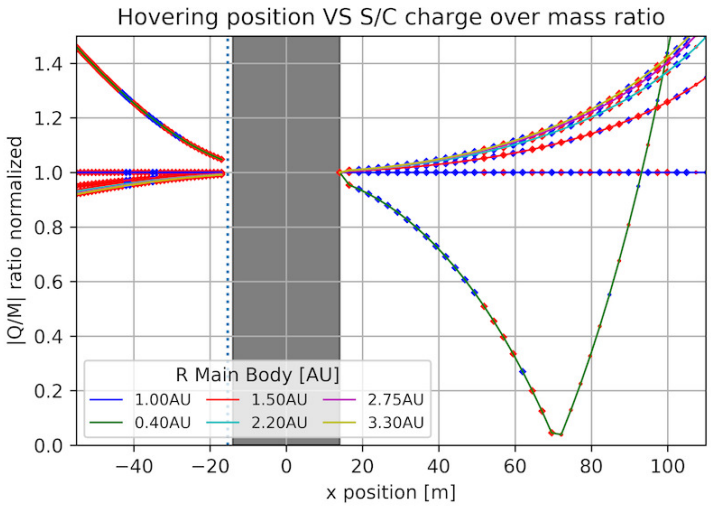

Fig. 15 Variation of normalized |Q/M| as function of the Asteroid position

The absolute values of the Q/M obtained for each planet are normalized by the absolute value of the Q/M computed for the reference case. Figure 15 indicates that the normalized $|Q/M|$ increases on the sunlit side in case of inner asteroid while it decreases in case of outer asteroids. Moreover, the increment is higher if compared to the decrements obtained in each case of outer asteroid. This is due to the strongest effect of the solar wind acting on the sunlit side. By moving away from the asteroid in the sun direction, the difference with the reference case increases by following an exponential law. On the dark side, the trend is opposite. For an inner asteroid, the Q/M needed switches from negative to positive closer to the surface with respect to both the reference case and the outer asteroids, thus there is a region (just before the transition) in which effectively the Q/M required is reduced in magnitude (see Fig. 16). Also in this case there is a second transition position located at about 105 meters (see Fig. 16) from the center of the asteroid, on the dark side region due to the inversion of the sign in E_x. Figure 16 confirms that the hovering on the sunlit regions requires higher level of charge for inner asteroids, while on the dark side the charge required for these asteroids is lower. The solar wind effects on the dark side hovering are quite low for an outer asteroid, since the $|Q/M|$ increment switching from 1.5 AU to 2.2 AU is much stronger than the one computed from 2.2 AU to 3.3 AU (see Fig. 15). The positions of

the stable equilibria are basically not changed with respect to the reference case (the legend for the equilibrium point is the same of the previous cases).

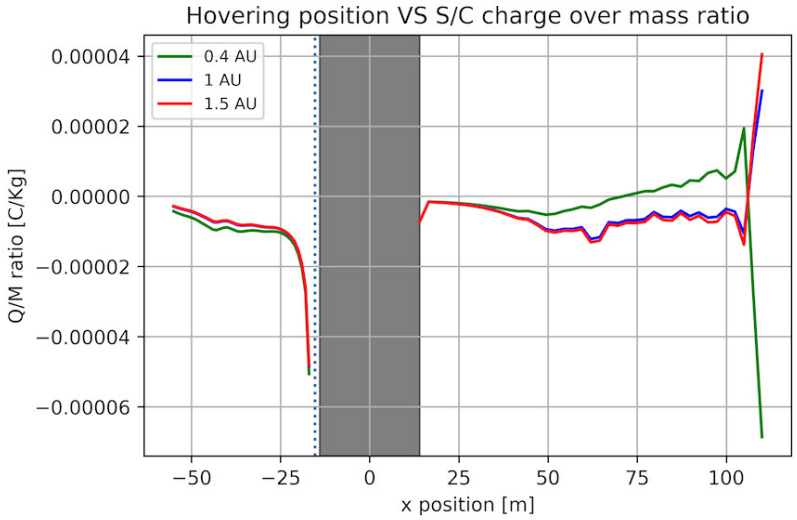

Fig. 16 Variation of Q/M as function of the Asteroid position

V. Conclusions

This paper discussed the models required to simulate the hovering mission phase of an E-Glider engaged in proximity operations around a small airless body, and determined the hovering operation requirements. The focus of the paper was on the analysis of the equilibrium points and of the hovering conditions in a fuel free mode, as enabled by using only electrostatic actuation. 3D fully kinetic PIC simulations were carried out to simulate the interactions of both the asteroid and the E-Glider with the solar wind plasma. The electrostatic force between E-Glider and asteroid was calculated utilizing the electric field obtained from PIC simulations for a range of the E-Glider charge to mass ratio.

The analysis of the zero velocity curves, i.e. the dynamic equilibria, indicates the existence of several equilibrium points. In particular, the coexistence of more than one non-collinear equilibrium point on the sunlit side both for $Q > 0$ and $Q < 0$, as well as the coexistence of both collinear and non-collinear points for the same level of charge, both on the sunlit side and on the dark side, was verified. These results are extremely important because they demonstrate that a simple plasma interaction model, such as the Nitter model, is not accurate enough to be used to describe the actual environment in close proximity of an asteroid with the level of confidence required for the evaluations of the feasibility of an E-Glider mission. The conclusions are also supported by the fact that the analysis of the subsolar hovering requires a charge lower than the one that can be predicted by using the Nitter model. By reducing the analysis to the subsolar hovering case, the charge-to-mass ratio needed to achieve the hovering condition at a given altitude can be obtained. This analysis points out that there are stable equilibrium points at about $10 - 100$ meters of altitude

which are achievable with a lower level of charge than the one predicted by using the Nitter model. The analysis of the hovering sensitivity with respect to the radius indicated that the charge-to-mass ratio needed to hover at a given position increases quadratically with the equivalent radius of the spacecraft. The analysis of the hovering sensitivity with respect to the small body position indicated that the required charge-to-mass ratio needed to hover on the sunlit face increases as the small body gets closer to the Sun.

This paper did not invoke a specific E-Glider design and charging mechanism. The net charging carried by E-Glider was treated as an input parameter. The E-Glider potential was assumed to be the floating potential under the average solar wind plasma condition. Under this assumption, the electrostatic force acted on the E-Glider was at the weakest for a given charge to mass ratio due to shielding by plasma sheath. An E-Glider in a stronger plasma charging environment or charged by artificial means can achieve a significantly higher potential, which can lead to a stronger electrostatic force and thus a more favorable hovering capability than that presented in this paper. We note that the E-Glider potential and power consumption are determined by the shape and the size of the electrodes, and limited by environmental conditions.

Future studies will need to address the E-Glider charging and extend the study of the equilibrium dynamics for a more complex spacecraft model which includes specific electrode designs and charging mechanisms. Based on the promising results obtained for the static electrostatic hovering analysis, an extension to the more complex case of a 3D electrostatic control law that can switch from one hovering condition to another should also be considered. The 3D domain implies 6 degrees of freedom of motion. Thus, three dipoles aligned with the axis in body frame do not ensure the full controllability of the E-Glider. A possible solution that can lead to the reduction of the number of electrodes needed would be to consider the interactions between electrodes that are not aligned on a single body axis, e.g. the effects of differentially charging the electrode located at +x in the BF frame together with the one in -y in BF frame would be a net force and a torque on the spacecraft not aligned nor with the x-axis nor with the y-axis. The control authority to guide an E-Glider in a fully 3D domain could be obtained by using different electric dipoles, but the control requirements and the minimum number of the electrodes needed remain to be carefully evaluated.

Acknowledgments

U.S. Government sponsorship acknowledged. This research was carried out at Jet Propulsion Laboratory, California Institute of Technology, under a contract with the National Aeronautics and Space Administration, during the internship sponsored by JVSRP (JPL Visiting Student Research Program). The reference project for the activity was the E-Glider concept, developed by Dr. Marco B. Quadrelli in the context of the NASA Innovative Advanced Concepts (NIAC) Program. We thank Chen Cui and William Yu of University of Southern California for help in generating PIC simulation data and Figs. 5 - 6.

References

[1] Quadrelli, M. B., Garrett, H., Castillo, J., Stoica, A., Ono, H., and Schaub, "NIAC Phase I Final Report - E-Glider: active electrostatic flight for airless body exploration," *NASA Innovative Advanced Concepts (NIAC)*, 2017. https://www.nasa.gov/sites/default/files/atoms/files/niac_2016_phasei_quadrelli_eglider_tagged.pdf.

[2] Morley, E. L., and Robert, D., "Electric Fields Elicit Ballooning in Spiders," *Current Biology*, Vol. 28, No. 14, 2018, pp. 2324–2330. https://doi.org/10.1016/j.cub.2018.05.057.

[3] Council, N. R., *Vision and Voyages for Planetary Science in the Decade 2013-2022*, The National Academies Press, Washington, DC, 2011. URL https://www.nap.edu/catalog/13117/vision-and-voyages-for-planetary-science-in-the-decade-2013-2022.

[4] Han, D., "Particle-In-Cell Simulations of Plasma Interaction with Asteroidal and Lunar Surfaces," Dissertation, University of South California, 2015. http://digitallibrary.usc.edu/cdm/ref/collection/p15799coll3/id/639389.

[5] Scheeres, D. J., Gaskell, R., Abe, S., Barnouin-Jha, O., and Hashimoto, T., "The Actual Dynamical Environment About Itokawa," *AIAA/AAS Astrodynamics Specialist Conference and Exhibit*, 2006. https://doi.org/10.2514/6.2006-6661.

[6] Nesnas, I. A., Matthews, J. B., Abad-Manterola, P., Burdick, J. W., Edlund, J. A., Morrison, J. C., Peters, R. D., Tanner, M. M., Miyake, R. N., Solish, B. S., and Anderson, R. C., "Axel and DuAxel rovers for the sustainable exploration of extreme terrains," *Journal of Field Robotics*, Vol. 29, No. 4, 2012, pp. 663–685. https://doi.org/10.1002/rob.21407, URL https://onlinelibrary.wiley.com/doi/abs/10.1002/rob.21407.

[7] Withrow-Maser, S., Koning, W., Kuang, W., and Johnson, W. R., "Recent Efforts Enabling Martian Rotorcraft Missions," *NASA Technical Reports Server (NTRS)*, 2020. URL https://ntrs.nasa.gov/archive/nasa/casi.ntrs.nasa.gov/20200000788.pdf.

[8] Scheeres, D., "Satellite Dynamics About Asteroids," *AAS/AIAA Spaceflight Mechanics Meeting*, 1994.

[9] Scheeres, D., *Orbital Motion In Strongly Perturbed Environments*, Vol. 1, Springer, 2012.

[10] Scheeres, D. J., "Satellite Dynamics about small bodies: Averaged Solar Radiation Pressure Effects," *Journal of the Astronautical Sciences*, Vol. 47, No. 1, 1999, pp. 25–46.

[11] Scheeres, D. J., and Marzari, F., "Spacecraft Dynamics in the Vicinity of a Comet," *Journal of the Astronautical Science*, Vol. 50, No. 1, 2002, pp. 35–52.

[12] Scheeres, D., "Orbit mechanics about small asteroids," *NASA Archive*, 2007. https://ntrs.nasa.gov/archive/nasa/casi.ntrs.nasa.gov/20080012725.pdf.

[13] Seeni, A., Schäfer, B., and Hirzinger, G., *Robot Mobility Systems for Planetary Surface Exploration – State-of-the-Art and Future Outlook: A Literature Survey*, Aerospace Technology Advancements, 2010, pp. 189–208. https://doi.org/10.5772/6930.

[14] Quadrelli, M. B., Mazhar, H., and Negrut, D., "Modeling and Simulation of Anchoring Processes for Small Body Exploration," *AIAA SPACE 2012 Conference & Exposition*, 2012, p. 5310.

[15] Schaub, H., Parker, G. G., and King, L. B., "Challenges and prospects of Coulomb spacecraft formation control," *Journal of Astronautical Sciences*, Vol. 52, No. 1, 2004, pp. 169–193.

[16] Aslanov, V., and Schaub, H., "Detumbling attitude control analysis considering an electrostatic pusher configuration," *Journal of Guidance, Control, and Dynamics*, Vol. 42, No. 4, 2019, pp. 900–909.

[17] King, B. L., Parker, G. G., Deshmukh, S., and Chong, J., "NIAC Phase I Final Report - Spacecraft Formation-flying using Inter-vehicle Coulomb Forces," *NASA Innovative Advanced Concepts (NIAC)*, 2002. http://www.niac.usra.edu/files/studies/final_report/601King.pdf.

[18] Lee, P., "Dust Levitation on Asteroids," *Icarus*, Vol. 124, No. 1, 1996, pp. 181 – 194.

[19] Whipple, E. C., "Potentials of surfaces in space," *Reports on progress in Physics*, Vol. 44, No. 11, 1981, pp. 1197–1250.

[20] Nitter, T., Havnes, O., and Melandsø, F., "Levitation and dynamics of charged dust in the photoelectron sheath above surfaces in space," *Journal of Geophysical Research: Space Physics*, Vol. 103, No. A4, 1998, pp. 6605–6620. https://doi.org/10.1029/97JA03523.

[21] Colwell, J. E., Gulbis, A. A., Horányi, M., and Robertson, S., "Dust transport in photoelectron layers and the formation of dust ponds on Eros," *Icarus*, Vol. 175, No. 1, 2005, pp. 159–169.

[22] Han, D., and Wang, J., "3-D Fully Kinetic Particle-in-Cell Simulations of Small Asteroid Charging in the Solar Wind," *IEEE Transactions on Plasma Science*, Vol. 47, No. 8, 2019, pp. 3682–3688. https://doi.org/10.1109/TPS.2019.2919895.

[23] Wang, J., and Hastings, D., "Ionospheric plasma flow over large high-voltage space platforms. II: The formation and structure of plasma wake," *Physics of Fluids B: Plasma Physics*, Vol. 4, No. 6, 1992, pp. 1615–1629.

[24] Wang, J., and Hu, Y., "The breakdown of the fluid approximation for electrons in a plasma wake," *Journal of Geophysical Research: Space Physics*, Vol. 123, No. 10, 2018, pp. 8797–8805.

[25] Hartzell, C. M., "The Dynamics of Near-Surface Dust on Airless Bodies," Dissertation, University of Colorado Boulder, 2012. https://scholar.colorado.edu/concern/graduate_thesis_or_dissertations/6w924c073.

[26] Jeong, H., "Kinetic Simulations of Spacecraft Charging and Plasma Interactions in the Solar Wind," Dissertation, Virginia Polytechnic Institute and State University, 2008. https://vtechworks.lib.vt.edu/bitstream/handle/10919/30237/Dissertation_Jeong.pdf?sequence=1&isAllowed=y.

[27] Quadrelli, M. B., Garrett, H., Castillo, J., Stoica, A., Ono, H., and Schaub, "Active electrostatic flight for airless body," *2017 IEEE Aerospace Conference*, 2017, pp. 1–16. https://doi.org/10.1109/AERO.2017.7943821.

[28] Kikuchi, S., "E-glider: Active Electrostatic Flight for Airless Body Exploration," Research report, The University of Tokyo, 2017.

[29] Han, D., Wang, J., and He, X., "A Nonhomogeneous Immersed-Finite-Element Particle-in-Cell Method for Modeling Dielectric Surface Charging in Plasmas," *IEEE Transactions on Plasma Science*, Vol. 44, No. 8, 2016, pp. 1326–1332. https://doi.org/10.1109/TPS.2016.2580698.

[30] Evlanov, E. N., Zavjalov, M. A., and Tyuryukanov, P. M., "Electron guns for spacecraft," *Cosmic Research*, Vol. 51, No. 5, 2013, pp. 388–395. https://doi.org/10.1134/S0010952513050043.

[31] Masek, T. D., and Cohen, H. A., "Satellite Positive-Ion-Beam System," *Journal of Spacecraft and Rockets*, Vol. 15, No. 1, 1978, pp. 27–33. https://doi.org/10.2514/3.57284.

[32] Lai, S. T., "An overview of electron and ion beam effects in charging and discharging to spacecraft," *IEEE Transactions on Nuclear Science*, Vol. 36, No. 6, 1989, pp. 2027–2032. https://doi.org/10.1109/23.45401.

[33] Marrese, C., Wang, J., Goodfellow, K., and Gallimore, A., "Space-Charge Limited Emission from Field Emission Array Cathodes for Electric Propulsion and Tether Applications," *Micropropulsion for Small Spacecraft, Progress in Aeronautics and Astronautics, AIAA*, Vol. 187, 2000, pp. 423–447.

[34] Wang, J., and Lai, S., "Virtual Anode in Ion Beam Emissions in Space: Numerical Simulations," *Journal of Spacecraft and Rockets*, Vol. 34, No. 6, 1997, pp. 829–836.

[35] Plis, E. A., Engelhart, D. P., Likar, J., Hoffmann, R. C., Cooper, R., and Ferguson, D., "Electrical Behavior of Carbon-Loaded Kapton for Spacecraft Applications," *Journal of Spacecraft and Rockets*, Vol. 55, No. 3, 2018, pp. 775–777. https://doi.org/10.2514/1.A33970.

[36] Czepiela, S. A., McManus, H., and Hastings, D., "Charging of composites in the space environment," *Journal of Spacecraft and Rockets*, Vol. 37, No. 5, 2000, pp. 556–560. https://doi.org/10.2514/2.3619.

[37] Mizera, P., "A summary of spacecraft charging results," *Journal of Spacecraft and Rockets*, Vol. 20, No. 5, 1983, pp. 438–443. https://doi.org/10.2514/3.25625.

[38] Peck, M., "Prospects and Challenges for Lorentz-Augmented Orbits," *Collection of Technical Papers - AIAA Guidance, Navigation, and Control Conference*, Vol. 3, 2005. https://doi.org/10.2514/6.2005-5995.

[39] Yu, W., Han, D., and Wang, J., "Numerical Simulations of Dust Dynamics Around Small Asteroids," *IEEE Transactions. Plasma Sciences*, Vol. 47, No. 8, 2019, pp. 3724–3730. https://doi.org/10.1109/TPS.2019.2920263.

[40] Corradino, F., "Modeling of orbital and attitude dynamics of a satellite controlled via active electrostatic charging," Tesi di laurea magistrale, Politecnico di Torino, 2018. https://webthesis.biblio.polito.it/6853/1/tesi.pdf.

[41] Curtis, H. D., *Orbital Mechanics for Engineering Students, 3rd Edition*, Elsevier, 2010.

[42] Gottlieb, R. G., "Fast Gravity, Gravity Partials, Normalized Gravity, Gravity Gradient Torque and Magnetic Field: Derivation, Code and Data," *Nasa Contractor Report 188243*, 1993. https://ntrs.nasa.gov/archive/nasa/casi.ntrs.nasa.gov/19940025085.pdf.

[43] Pines, S., "Uniform Representation of the Gravitational Potential and its Derivatives," *AIAA Journal*, Vol. 11, No. 10, 1973, pp. 1508–1511. https://doi.org/10.2514/3.50619.

[44] Eckman, R. A., Brown, A. J., and Adamo, D. R., "Normalization of Gravitational Acceleration Models," *NASA Scientific and Technical Information*, 2011. https://ntrs.nasa.gov/archive/nasa/casi.ntrs.nasa.gov/20110023121.pdf.

[45] Lundberg, B. J., "Recursion Formulas of Legendre Functions for Use with Nonsingular Geopotential Models," *Journal of Guidance, Control, and Dynamics*, Vol. 11, No. 1, 1988, pp. 31–38. https://doi.org/10.2514/3.20266.

[46] Lyon, H. R., "Geosynchronous Orbit Determination Using Space Surveillance Network Observations and Improved Radiative Force Modeling," Master degree thesis, Massachusetts Institute of Technology, 2004. https://dspace.mit.edu/handle/1721.1/17779.

[47] Han, D., Wang, J., and He, X., "Immersed-Finite-Element Particle-in-Cell Simulations of Plasma Charging at the Lunar Terminator," *Journal of Spacecraft and Rockets*, Vol. 55, No. 6, 2018, pp. 1490–1497. https://doi.org/10.2514/1.A34002.

[48] Wang, J., He, X., and Cao, Y., "Modeling Electrostatic Levitation of Dust Particles on Lunar Surface," *IEEE Transaction*, Vol. 36, No. 5, 2008, pp. 2459–2466.

[49] Cui, C., and Wang, J., "Numerical Simulations of Plasma-Spacecraft Interactions near Irregularly Shaped Small Asteroids," *Applied Space Environments Conference, Los Angeles, CA, May 13-17*, 2019.

[50] Wang, J., Leung, P., Garrett, H., and Murphy, G., "Multibody-Plasma Interactions: Charging in the Wake," *Journal of Spacecraft and Rockets*, Vol. 31, No. 5, 1994, pp. 889–894.

[51] Broschart, S. B., and Scheeres, D. J., "Control of Hovering Spacecraft Near Small Bodies: Application to Asteroid 25143 Itokawa," *Journal of Guidance, Control, and Dynamics*, Vol. 28, No. 2, 2005, pp. 343–354. https://doi.org/10.2514/1.3890.

[52] Kominato, T., Matsuoka, M., Uo, M., Hashimoto, T., and Kawaguchi, J., "Optical hybrid navigation and station keeping around Itokawa," *AIAA/AAS Astrodynamics Specialist Conference and Exhibit*, 2006, p. 6535.

[53] Finckenor, M. M., "Multilayer Insulation Material Guidelines," *National Aeronautics and Space Administration*, 1999. https://ntrs.nasa.gov/archive/nasa/casi.ntrs.nasa.gov/19990047691.pdf.

[54] Fantino, E., and Casotto, S., "Methods of harmonic synthesis for global geopotential models and their first-, second- and third-order gradients," *Journal of Geodesy*, Vol. 83, No. 7, 2009, pp. 595–619. https://doi.org/10.1007/s00190-008-0275-0.